RESEARCH ARTICLE | FEBRUARY 07 2019

Sound radiation by supersonic unstable modes in hypersonic blunt cone boundary layers. I. Linear stability theory

Carleton P. Knisely ; Xiaolin Zhong

Physics of Fluids 31, 024103 (2019)
https://doi.org/10.1063/1.5055761
CHORUS

Physics of Fluids ARTICLE scitation.org/journal/phf

Sound radiation by supersonic unstable modes in hypersonic blunt cone boundary layers. I. Linear stability theory

Cite as: Phys. Fluids 31, 024103 (2019); doi: 10.1063/1.5055761
Submitted: 10 September 2018 • Accepted: 23 October 2018 •
Published Online: 7 February 2019

Carleton P. Knisely[a] and Xiaolin Zhong[b]

AFFILIATIONS

MAE Department, University of California, Los Angeles, California 90095, USA

[a]Electronic mail: carleton.knisely@gmail.com
[b]Electronic mail: xiaolin@seas.ucla.edu

ABSTRACT

There has been renewed interest in supersonic modes in hypersonic boundary layers, which have been previously thought to be insignificant due to their smaller amplitudes than Mack's traditional second mode. Supersonic modes are associated with an unstable second mode synchronizing with the slow acoustic spectrum, causing sound to radiate outwards from the boundary layer. Because supersonic modes have not been observed experimentally, the majority of previous investigations either relied on Linear Stability Theory (LST) to study supersonic modes on a flat plate or observed them in the context of other research objectives. This two-part study uses a combined LST and Direct Numerical Simulation (DNS) approach to investigate the mechanism of supersonic modes in Mach 5 flow over a blunt cold-wall cone with thermochemical nonequilibrium effects. Paper I focuses on LST with new shock boundary conditions, whereas Paper II [C.P. Knisely and X. Zhong, "Sound radiation by supersonic unstable modes in hypersonic blunt cone boundary layers. II. Direct numerical simulation," Phys. Fluids **31**, 024104 (2019)] focuses on DNS with the overall goal of investigating the impact of supersonic modes on transition. LST results indicate that supersonic modes exist in the flow with wall-to-free-stream temperature ratio $T_w/T_\infty = 0.2$ and create an abnormal growth pattern. However, supersonic modes were not shown to exist using LST in the case with $T_w/T_\infty = 0.667$. Subsequent DNS analysis in Paper II shows supersonic modes in the $T_w/T_\infty = 0.667$ case, although they are significantly weaker than the second mode and are unlikely to lead to transition. Understanding the mechanism of supersonic modes can yield more accurate transition location predictions leading to improved estimates for drag and heat transfer to the vehicle.

I. INTRODUCTION

It has long been known that boundary layer transition from laminar to turbulent has a considerable impact on the design of hypersonic vehicles.[1–3] Transition to turbulent flow drastically increases drag and heating to the vehicle surface and can have a prominent effect on control of the hypersonic vehicle. It also affects engine performance and operability as well as vehicle structure and weight. The heating to the vehicle surface is one of the primary considerations in hypersonic vehicle design. Thermal protection systems (TPSs) are required to prevent the surface of the vehicle from overheating and failing. TPSs are usually specified with a large factor of safety to ensure protection of the vehicle, although this often adds unnecessary weight, reducing the maximum payload. The ability to predict accurately or even to delay the onset of transition and to maintain laminar flow can have a significant payoff in terms of the reduction in aerodynamic heating, higher fuel efficiency, and weight of the thermal protection system.

Mack[4] found that the major instability waves leading to transition to turbulence in hypersonic flow are the first and second modes, although it should be noted that these instabilities are not distinctive modes in the mathematical definition.[5] For a linear disturbance in a variable q, its perturbation can be described by

$$q' = \hat{q}(y)\exp[i(\alpha x + \beta z - \omega t)], \quad (1)$$

where $\hat{q}(y)$ is the eigenfunction, ω is the circular frequency of the disturbance, and α and β are the wavenumbers. For a 2D disturbance, $\beta = 0$. Commonly, ω and β are assumed to be real and the wavenumber α is assumed to be complex, which means that the disturbances grow in space, resulting in a spatial stability analysis. If ω is complex and α and β are real, then the disturbances grow in time, resulting in a temporal stability analysis. When ω is real, the speed of the disturbance propagation in space is related to the real component of the wavenumber via the phase speed, $c_r = \omega/\alpha_r$, with the negative of the imaginary component representing the growth rate. Therefore, for a neutral disturbance all wavenumbers are real.

Assuming neutral instabilities, the second mode has been visualized as acoustic rays physically trapped between the wall and the sonic line by Morkovin[6] in 1987, Mack[7] in 1990, Reshotko[1] in 1991, and later by Fedorov[3] in 2011. Mack[7] also noted that the second mode (and higher acoustic modes) is present, whenever there is a region of local supersonic flow relative to the phase speed of the instability wave between the wall and the relative sonic point. It is instructive to examine a schematic for the second mode with acoustic-like behavior for comparison to 2D Linear Stability Theory (LST) and Direct Numerical Simulation (DNS) contours. An illustration similar to Morkovin's,[6] Mack's,[7] Reshotko's,[1] and Fedorov's,[3] which assumes the large wavenumber limit of a neutral mode, is shown in Fig. 1. However, for non-neutral second mode waves, the physical picture is less obvious,[7] although one would expect a qualitatively similar physical illustration for weakly non-neutral waves despite being quantitatively different. Including the imaginary component of the wavenumber can be thought of as a damping effect. The development of such a visualization of the second mode requires the understanding of the role of the sonic line in the hypersonic boundary layer stability equations.

A useful parameter describing the speed of propagation of the disturbance relative to the mean flow is the complex local relative Mach number

$$\overline{M}(y) = \frac{\overline{u}(y) - c}{\overline{a}(y)}, \tag{2}$$

where $\overline{u}(y)$ is the local mean flow velocity tangential to the wall, $c = \omega/\alpha$ is the complex disturbance propagation speed with ω being the circular frequency, α is the streamwise wavenumber, and $\overline{a}(y)$ is the local mean flow speed of sound. The real component of the phase speed is denoted as c_r. The local relative Mach number appears in the nondimensional stability equations, as presented by Mack[4] in his Eq. (9.8),

$$D^2\left[\hat{v}/(\tilde{\alpha}\tilde{U} - \omega)\right] + D\left\{\ln\left[\frac{\overline{M}^2}{1-\overline{M}^2}\right]\right\} D\left[\hat{v}/(\tilde{\alpha}\tilde{U} - \omega)\right] - \tilde{\alpha}^2(1-\overline{M}^2)\left[\hat{v}/(\tilde{\alpha}\tilde{U} - \omega)\right] = 0, \tag{3}$$

where $D = d/dy$, $\hat{v}$ is the wall-normal velocity complex eigenfunction, $\tilde{\alpha}\tilde{U} = \alpha U + \beta W$, where α and β are the streamwise and spanwise complex wavenumbers, respectively, and U and W are the streamwise and spanwise mean flow velocities, respectively, $\tilde{\alpha}^2 = \alpha^2 + \beta^2$, and ω is the complex frequency.

Taking the large wavelength limit of Eq. (3) allows for an analytical solution to be obtained by the WKB method.[4] Making this simplification results in Mack's[4] Eq. (9.16),

$$D^2\left[\hat{v}/(\tilde{\alpha}\tilde{U} - \omega)\right] - \tilde{\alpha}^2(1-\overline{M}^2)\left[\hat{v}/(\tilde{\alpha}\tilde{U} - \omega)\right] = 0. \tag{4}$$

It must be noted that Mack's[4] original Eq. (9.16) included a typo and should not be copied directly. From Eq. (4), it is clear that there is a turning point as $|\overline{M}|$ increases past unity. The solution of the second order ordinary differential equation (ODE) changes its behavior at the turning point, resulting in the different nature of the solution depending on the value of $\overline{M}$. However, it must be noted that the second mode actually does not strictly satisfy Eq. (4) due to the limiting case assumption of a large $\tilde{\alpha}^2$ wavenumber.[8] For a finite wavenumber, the extra first derivative term appears in Eq. (3). In the limit of large wavenumber, the simplified Eq. (4) becomes exact for the second mode; however, in reality it is only approximate.

The relative sonic line, or turning point (denoted here as y_s), described by Morkovin,[6] Mack,[7] Reshotko,[1] and Fedorov[3]

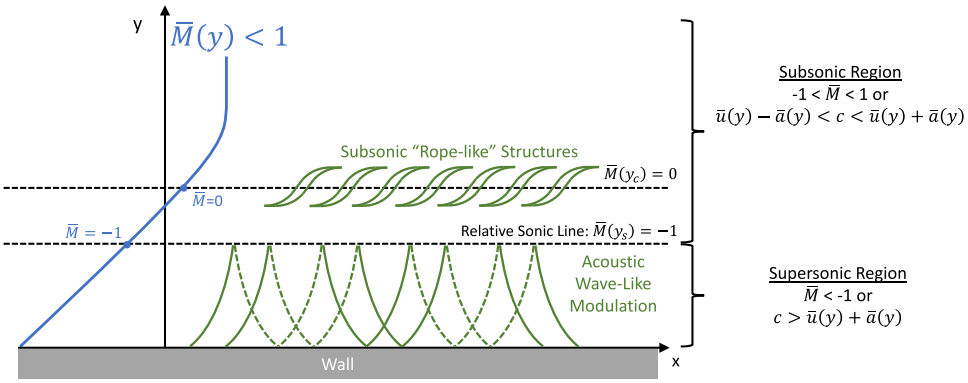

FIG. 1. Visualization of neutral second mode similar to Morkovin's,[6] Mack's,[7] Reshotko's,[1] and Fedorov's[3] assuming a large wavenumber. The sonic line is denoted by $\overline{M}(y_s) = -1$, and the critical layer is by $\overline{M}(y_c) = 0$. The reflection at the sonic line changes waves from compression to expansion and vice versa.

for a neutral mode is then given by $\overline{M}(y_s) = -1$ or $c = \overline{u}(y_s) + \overline{a}(y_s)$ in Fig. 1. More generally, the relative sonic line can be defined as any location where the magnitude of the real component of the relative Mach number is equal to unity, i.e., $|Real(\overline{M})| = 1$. Near the wall, the disturbance is propagating downstream supersonically ($\overline{M} < -1$) with respect to the local mean flow velocity. In this region where $\overline{M} < -1$, the solution to the stability equations is acoustic-like, resulting in the acoustic disturbance waves trapped by the wall with the relative sonic line acting as a wave guide in the large wavenumber limit. Outside of the $\overline{M} = -1$ turning point at $y = y_s$, the disturbance is traveling subsonically with respect to the free stream and creates a "rope-like" wave pattern observed by many researchers both experimentally[9,10] and numerically.[11–13] These structures are centered about $\overline{M}(y_c) = 0$, or equivalently $c = \overline{u}(y_c)$, with y_c denoting the critical layer. Because the phase speed of the mode is subsonic in the freestream, i.e., $\overline{M} < 1$ such a mode is referred to as a subsonic mode. The new illustration of the second mode in Fig. 1 is presented rather than the classical schematics[1,3,6,7] in preparation of a new illustration of the supersonic mode based on the same principles.

The nomenclature for hypersonic boundary layer instability modes has evolved throughout the decades, so it is pertinent to describe the first and second modes with respect to Fedorov and Tumin's[5] contemporary notation using mode S and mode F1 in conjunction with the continuous modes; the fast and slow acoustic, entropy, and vorticity spectra. Mode S and mode F1 are discrete modes that originate in the slow and fast acoustic spectra at the leading edge of the body. That is, mode S begins with a phase speed $c_r = 1 - 1/M_\infty$ and mode F1 begins with a phase speed of $c_r = 1 + 1/M_\infty$. In typical supersonic flows, the interaction of mode S with the slow acoustic spectrum can cause mode S to become unstable. This first unstable mode is referred to as Mack's first mode and is a viscous instability[4] and is the compressible analog of Tollmien-Schlichting waves. In hypersonic flows, however, due to the increased Mach number, the viscous instability is insignificant and can be completely stabilized. Further downstream from the leading edge, mode S increases in phase speed while mode F1 decreases in phase speed. Eventually mode S and mode F1 synchronize, defined here as both modes having equal phase speeds, regardless of the growth rate. During synchronization, one mode can become unstable, while the other is stabilized.[5] Typically, mode S is the unstable mode, although under certain flow conditions mode F1 can become unstable instead.[14] Regardless of which mode is unstable, Mack's second mode refers to the unstable mode occurring after synchronization between mode F1 and mode S. Mack[4] referred to an infinite number of higher unstable modes in hypersonic flows. Indeed, there are additional fast acoustic discrete modes that occur farther downstream, denoted as modes F2, F3, etc. These higher modes follow a similar pattern to mode F1 in that they originate in the fast acoustic spectrum and decrease in phase speed downstream. Mode F2 eventually synchronizes phase speed with mode S (downstream of the mode F1/S synchronization location), which can again result in an unstable mode. In general, this unstable mode is mode S and is referred to as Mack's third mode. Similarly, synchronization of mode F3 with mode S can result in Mack's fourth mode. The third and higher modes are decreasing in amplitude from the second mode;[4] therefore, the focus of the majority of hypersonic boundary layer transition studies is on the second mode.

Researchers have developed numerical tools to predict transition to turbulence due to the first and second modes. Malik[15] implemented multiple numerical methods for solving the LST equations for a perfect gas. Chemical nonequilibrium effects in the LST framework were studied numerically by Stuckert and Reed.[16] Hudson *et al.*[17] incorporated thermal nonequilibrium effects in addition to chemical nonequilibrium for LST. Johnson *et al.*[18–20] studied hypersonic boundary layer transition in thermochemical nonequilibrium using the Parabolized Stability Equations (PSE), which account for nonparallel flow effects that are ignored in LST. Overall, the researchers determined that the dissociation of air species is stabilizing to the first mode but destabilizing to the second mode. Additionally, it was determined that thermal nonequilibrium has a slight destabilizing effect on the first mode, and a slight stabilizing effect on the second mode.

When the traditional mode S is the unstable second mode, its phase speed is subsonic, i.e., $1 - 1/M_\infty < c_r < 1 + 1/M_\infty$. Although most hypersonic boundary layer transition studies have primarily focused on the second mode in which mode S is unstable, it has been shown that when mode F1 is unstable, there can be synchronization between mode F1 and the slow acoustic spectrum downstream of the mode F1/S synchronization location.[7,21] That is, the unstable second mode (F1) can synchronize with the slow acoustic spectrum, causing a peculiarity in the eigenvalue spectrum due to the proximity of a discrete mode to a continuous mode. Downstream of this synchronization with the slow acoustic spectrum, the unstable mode F1 has a supersonic phase speed, i.e., $c_r < 1 - 1/M_\infty$. When this situation occurs, the unstable mode F1 is referred to as the supersonic mode, and it is associated with unique features not present in traditional flows with a subsonic second mode. Specifically, the supersonic mode is characterized by a second region of relative supersonic flow outside of the critical layer, resulting in the radiation of sound from the boundary layer.

Although early studies by Mack in 1985[21] and 1990[7] and Reshotko in 1991[1] came to the consensus that the supersonic mode was insignificant due to its smaller disturbance amplification rate than the second mode, there has been renewed interest in studying the supersonic mode in hypersonic boundary layers due to their presence in the flow conditions typical of the T5 shock tunnel at Caltech. In such high-enthalpy shock tube experiments, the wall temperature remains ambient during the short test duration, resulting in a cold wall with respect to the free stream. Cold wall conditions in high-enthalpy flows are also found in some real flight cases.[22,23] It has long been known through studies by

Lees[24] and Mack[21,25] that wall cooling stabilizes the first mode but destabilizes the second mode. Bitter and Shepherd[26] in 2015 took these studies a few steps further and have shown through a chemical equilibrium, thermal nonequilibrium LST analysis that high levels of wall cooling on a flat plate lead to unique features, in particular an unstable second mode traveling upstream supersonically relative to the free stream. The supersonic modes are associated with instabilities over a wider range of frequencies than subsonic modes during which acoustic waves radiate from the wall into the free stream. This phenomenon has also been referred to as the spontaneous radiation of sound by Fedorov.[27,28]

Despite the existence of the supersonic mode being known since the mid-1980s by Mack[7,21] and Reshotko in the early 1990s,[1] a comprehensive examination of its impact on transition to turbulence is yet to be performed. There have been only a few studies in which the supersonic mode's characteristics were the direct focus of the investigation. In 1997, Chang, Vinh, and Malik[29] reported supersonic modes in Mach 20 chemical nonequilibrium, thermal equilibrium flow over a 6° wedge with wall temperature ratio T_w/T_{ad} = 0.1, and noted that the stability boundary conditions in the free stream are critical to resolving the supersonic mode due to its oscillatory nature in the free stream. Additionally, they noted that peak species perturbation coincides with the location of maximum chemical production in the boundary layer, and therefore the species eigenfunctions do not oscillate in the free stream, whereas pressure, temperature, and velocity perturbations exhibit the oscillatory behavior outside of the boundary layer. Over a decade later came a resurgence of the supersonic mode; however, in most cases it was not the primary focus of the study. In 2011, Fedorov *et al.*[30] encountered unstable supersonic modes in flow with resonating micro-cavities on a flat plate. Wagnild[31] observed the spontaneous radiation of sound in 2012 on a 5° half-angle sharp cone, although the focus of his study was the effect of vibrational nonequilibrium on boundary layer stability. In 2013, Bres *et al.*[32] also found this phenomenon in flow over a wall with a porous coating on a flat plate. Klentzman and Tumin[33] in 2013 also commented on the supersonic mode in a cold-wall flat plate flow using oxygen. Jewell[34] in 2014 performed numerical calculations to supplement experimental results from the T5 tunnel at Caltech. Jewell's numerical results showed the supersonic mode on a 5° half-angle sharp cone, although the focus of his dissertation was transition delay with CO_2 concentration, turbulent spot propagation, and transition control via gas injection. In the same year, Fedorov, Soudakov, and Leyva[35] found unstable supersonic modes on a 5° half-angle cone with gas injection. Over the course of 2014-2016, Salemi *et al.* also modeled the 5° half-angle sharp cone configurations typical of the T5 tunnel at Caltech and investigated second mode synchronization with the slow acoustic spectrum. They investigated the effect of nonlinear disturbances,[36,37] a flared cone geometry,[38] and high-temperature effects,[39] although the Prandtl number and ratio of specific heats were fixed in their real gas model. Overall, Salemi[40] concluded that the synchronization of mode F1 with the slow acoustic spectrum caused the emission of acoustic waves from the boundary layer into the free stream. In 2017, the results of Sescu *et al.*[41] were indicative of the supersonic mode in cold-wall flat plate flow, although the focus of the study was the effect of surface deformations on boundary layer stability.

A contemporary study directly focusing on the supersonic mode was performed in 2015 by Bitter and Shepherd,[26] who provided clear evidence through LST of the supersonic mode's existence on a cold-wall flat plate, although they neglected chemical nonequilibrium effects. Bitter and Shepherd also demonstrated that the cause of the supersonic mode was the synchronization of mode F1 with the slow acoustic spectrum that occurred on highly cooled walls. The following year in 2016 Chuvakhov and Fedorov[27,28] largely confirmed Bitter and Shepherd's[26] findings through perfect gas LST analysis as well as unsteady DNS analysis on a flat plate, although they used different free stream conditions. Edwards and Tumin[42] in 2017 found the supersonic mode on a hot wall with chemical effects, upending the notion that the supersonic mode occurs only on highly cooled walls. Edwards and Tumin incorporated additional source terms in their mean flow equations accounting for kinetic fluctuations in the flow but used a perfect gas stability solver. Edwards and Tumin suggested that these kinetic fluctuations may generate a discrete mode in the vicinity of the neutral point. Depending on the flow parameters, the excited mode can become supersonic far downstream in the vicinity of the upper neutral branch curve. Therefore, the effect of wall temperature on the supersonic mode in thermochemical nonequilibrium flow must be re-evaluated. In 2018, Knisely and Zhong[43] performed thermochemical nonequilibrium LST and DNS studies using similar hot wall flow conditions on a 5° half-angle blunt cone and confirmed the existence of the supersonic mode, although it was quite weak. Knisely and Zhong[44] later in 2018 showed with unsteady DNS that the cold wall is destabilizing to the supersonic mode so much so that it is possible for the supersonic mode to have a greater magnitude than the traditional second mode. Furthermore, Mortensen[45] in 2018 discovered the supersonic mode in Mach 20 thermochemical nonequilibrium flow over very blunt cones and determined the supersonic mode to have a significantly higher amplitude than the second mode for nose radii greater than approximately 36 mm. Such a finding is novel and raises concerns of a dominant supersonic mode existing in other seldomly studied (but still practically relevant) flows. Therefore, a comprehensive examination of the supersonic mode's impact on transition to turbulence must be performed.

A schematic of a neutral supersonic mode (similar to the one developed by Knisely and Zhong[46]) is presented in Fig. 2 for further elaboration based on the same argument as the neutral subsonic second mode in Fig. 1, except a second relative sonic line is included. Specifically, it must again be noted that the visualization presented here is developed for the limiting case of a large wavenumber neutral mode, although there are qualitative similarities for finite wavenumber non-neutral

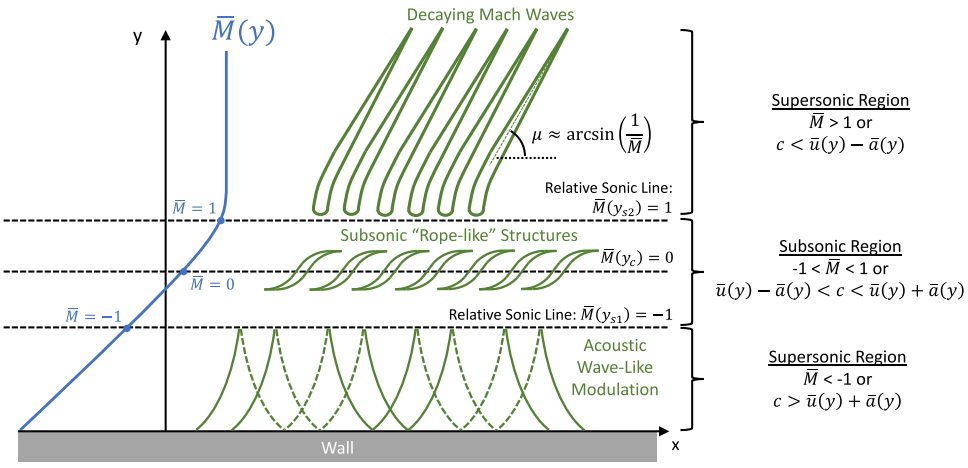

FIG. 2. Visualization of neutral supersonic mode in a large wavenumber limit. The first sonic line is denoted by $\overline{M}(y_{s1}) = -1$, the critical layer is by $\overline{M}(y_c) = 0$, and the second sonic line is by $\overline{M}(y_{s2}) = 1$. The reflection at the first sonic line changes waves from compression to expansion and vice versa.

modes. Nevertheless, it is indicative of the results one might expect to obtain from LST, DNS, or experiments in future studies. Near the wall, the same structures exist as in the traditional subsonic second mode. The disturbance is traveling downstream supersonically relative to the mean flow, indicated below a relative Mach number of $\overline{M} < -1$, or equivalently $c > \bar{u}(y) + \bar{a}(y)$. The first sonic line $\overline{M}(y_{s1}) = -1$ again acts as a wave guide for the acoustic rays. Similar to the traditional subsonic second mode, outside of $\overline{M}(y_{s1}) = -1$, the disturbance is traveling subsonically with respect to the free stream and creates the "rope-like" wave pattern centered about the critical layer $\overline{M}(y_c) = 0$. When the phase speed of the disturbance is slow enough under very particular flow conditions, a second supersonic region can be present. There can exist a second relative sonic line $\overline{M}(y_{s2}) = 1$, or equivalently $c < \bar{u}(y_{s2}) - \bar{a}(y_{s2})$, outside of which the disturbance is traveling *upstream* supersonically with respect to the free stream. Again, because $|\overline{M}| > 1$, the solution is wave-like. This creates the "slanted" wave pattern outside of the boundary layer shown in the schematic in Fig. 2. As $y \to \infty$, the disturbance will reduce back to a pure acoustic wave. The angle created by this decaying wave pattern is analogous to a Mach wave angle from traditional compressible flow theory and is approximated by $\mu \approx \arcsin(1/\overline{M})$. For a neutral supersonic wave, this relation is exact. However because a non-neutral wave will have an imaginary component of the wavenumber, the Mach wave angle for a non-neutral instability will have a slightly different angle. Again, the schematic in Fig. 2 is simply an extension of the well-established visualization for the traditional subsonic second mode in the large wavenumber limit to include a second relative sonic line. In reality, the supersonic mode has a finite wavenumber and the extra first derivative term appears in Eq. (3). In the limit of large wavenumber, the simplified Eq. (4) becomes exact for the supersonic mode as well as the traditional subsonic second mode; however, in reality it is only an approximate relation used for instructive purposes.

The schematics of the subsonic second mode (Fig. 1) and the supersonic mode (Fig. 2) are simplified representations of the LST results of Bitter and Shepherd[26] and Knisely and Zhong.[46] Knisely and Zhong's[46] results are shown in Fig. 3 for further clarification. Near the wall below the $\overline{M} = -1$ sonic line, the disturbance is traveling supersonically downstream with respect to the mean flow. This is evident by the alternating red and blue wave patterns in both the subsonic mode [Fig. 3(a)] and the supersonic mode [Fig. 3(b)]. Outside of the first sonic line, both the subsonic and supersonic modes demonstrate the "rope-like" pattern centered about the critical layer at $\overline{M} = 0$. The relative Mach number for the subsonic mode [Fig. 3(a)] does not exceed unity in the freestream and strongly resembles the subsonic second mode diagram in Fig. 1. The relative Mach number of the supersonic mode [Fig. 3(b)], on the other hand, exceeds unity in the freestream. The disturbance is traveling upstream supersonically with respect to the mean flow, resulting in the acoustic-like wave pattern. Again, as $y \to \infty$, this would be a pure acoustic wave.

This description of the supersonic mode is also in agreement with Mack's[21] description of the supersonic mode. Mack commented on neutral supersonic waves in flow over a flat plate and further described the phenomenon as a region of local supersonic flow relative to the disturbance phase speed outside of the boundary layer.[7] As Mack stated in scenario (3) on p. 106 of Ref. 7, "There can be supersonic neutral solutions (i.e., $c_{phx} < 1 - 1/\tilde{M}_1$) which, in the free stream, are either pure outgoing, or pure incoming, Mach waves of the flow relative to the phase speed. These solutions are supersonic acoustic modes, because... they require an embedded region of locally supersonic relative flow within the boundary layer that is distinct from the outer supersonic relative flow." This scenario that Mack described is exactly the physical basis for the schematic introduced in Fig. 2 and agrees with the results of Knisely and Zhong[46] in Fig. 3.

In summary, the supersonic mode diagram developed here is simply an extension of the same principles used by

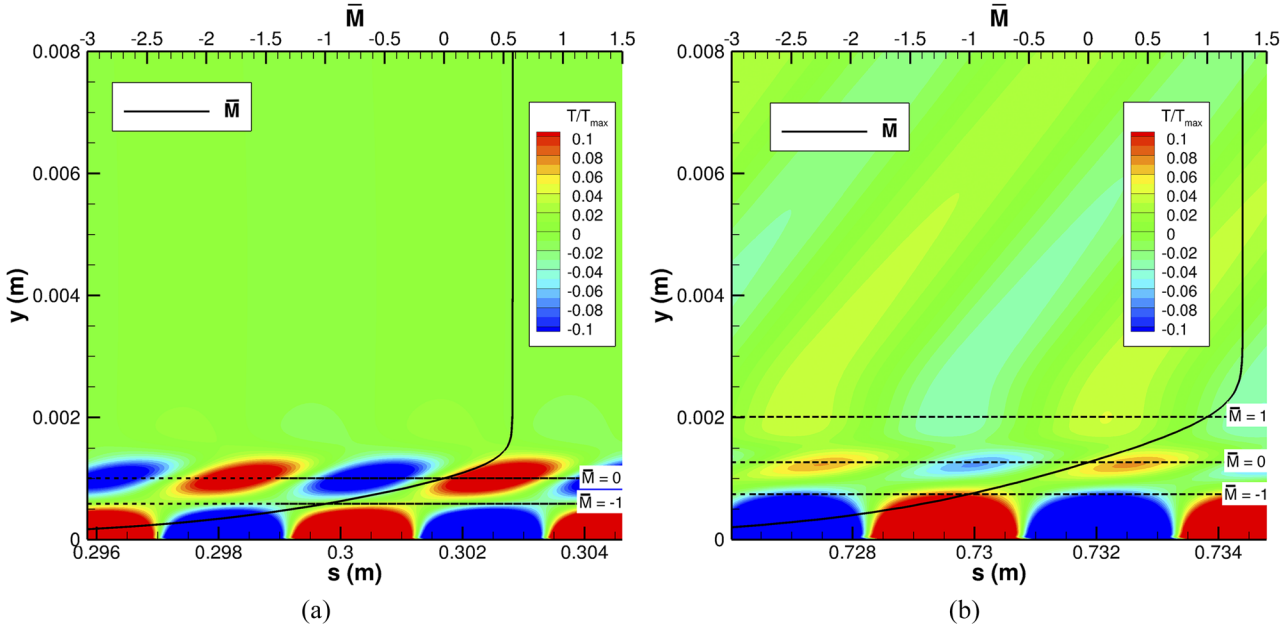

FIG. 3. Normalized contours of temperature fluctuations with relative Mach number $\overline{M}(y) = \frac{\bar{u}(y)-c_r}{\bar{a}(y)}$ overlaid (the solid black line corresponding to the top axis). T_w/T_∞ = 0.2, T_w = 300 K, M_∞ = 5: (a) Subsonic mode: c_r = 0.871 > 1 − 1/M_∞ at s = 0.302 m and f = 800 kHz. (b) Supersonic mode: c_r = 0.719 < 1 − 1/M_∞ at s = 0.733 m and f = 550 kHz. Reproduced with permission from C. Knisely and X. Zhong, "An investigation of sound radiation by supersonic unstable modes in hypersonic boundary layers," AIAA Paper 2017-4516, 2017. Copyright 2017 American Institute of Aeronautics and Astronautics, Inc.[46]

Morkovin,[6] Mack,[7] Reshotko,[1] and Fedorov[3] in their development of a subsonic second mode schematic that has been invaluable over the past 30+ years. The limiting case of the large wavenumber assumption is useful to obtain an analytical expression, demonstrating the trapped acoustic wave behavior. However, because this is a limiting case, in reality the second mode does not follow the simplified equation assuming a large wavenumber, i.e., the first derivative term in the stability equations cannot be neglected, making the physical picture less obvious. That being said, qualitatively the illustration will be similar. The supersonic mode diagram simply includes a second relative sonic line to the well-established diagrams.[1,3,6,7] Rather than having a single supersonic region and an outer subsonic region, the supersonic mode has two supersonic regions—one near the wall and the other outside of the critical layer. As $y \to \infty$, this would be a pure acoustic wave in the free stream. The traditional subsonic second mode diagram is still valid (as are those of Morkovin,[6] Mack,[7] Reshotko,[1] and Fedorov[3]), and therefore the supersonic mode diagram is valid as well because it is an extension of the original diagrams including a second sonic line.

Despite the evidence presented by Bitter and Shepherd[26] and Chuvakhov and Fedorov,[27,28] it is possible that the impact of the highly cooled wall on the spontaneous radiation of sound may have been overstated because chemical nonequilibrium was not accounted for. The recent theoretical results by Tumin[47] and Edwards and Tumin[42] in 2017 indicate the spontaneous radiation of sound in flows with $T_w/T_e > 1$. In addition, in 2018 Knisely and Zhong[43] performed thermochemical nonequilibrium LST and DNS studies using similar hot wall flow conditions on a 5° half-angle blunt cone and confirmed the existence of the supersonic mode, although it was quite weak. This phenomenon may be attributed to the real gas effect and may have been overlooked in previous simulations assuming chemical equilibrium.

This study performs a two-part in-depth analysis of the supersonic mode incorporating real gas effects on a blunt cone. Paper I focuses on LST, whereas Paper II focuses on DNS. It is critical to performing both analyses when studying the supersonic mode because results here and by Knisely and Zhong[43,44] indicate that the supersonic mode may be excited via a modal interaction that is not accounted for in LST. Therefore, to more accurately model the supersonic mode, full DNS studies to compliment LST predictions are necessary. In addition, as part of the investigation new less-restrictive LST equations and new LST shock boundary conditions are derived and verified. The goals are to use thermochemical nonequilibrium analysis to (1) determine the characteristics of the supersonic mode and under what conditions it exists and (2) examine the impact of the supersonic mode on transition to turbulence under realistic flight or experimental conditions.

II. SIMULATION CONDITIONS

The flow conditions for both simulations considered this study are intended to be similar to those used by Bitter and

TABLE I. Freestream flow conditions for direct numerical simulations.

Parameter	Value	Parameter	Value
M_∞	5	$H_{0,\infty}$	9.17 MJ/kg
ρ_∞	2.322×10^{-2} kg/m^3	p_∞	10 kPa
T_∞	1500 K	U_∞	3882.42 m/s
c_{N_2}	0.78	c_{O_2}	0.22

Shepherd[26] and are summarized in Table I. Two different mean flow cases are considered in this study; the only difference between the two cases is the isothermal wall temperature. All free stream conditions are identical. Case 1 had a wall temperature of T_w = 300 K, resulting in a wall-temperature ratio of T_w/T_∞ = 0.2. Case 2 had a wall temperature of T_w = 1000 K, resulting in a wall-temperature ratio of T_w/T_∞ = 0.667. Note the use of T_w/T_∞ rather than T_w/T_{aw} as used in many studies. The free stream temperature T_∞ was used instead because T_{aw} varies in the streamwise direction in the simulations. Using T_∞ results in a constant parameter characterizing the whole flow field.

The flow conditions for this study are intended to confirm that the DNS and LST methods were capable of producing the same physical artifacts on a blunt cone observed by Bitter and Shepherd[26] on a flat plate, and expand on the results of Knisely and Zhong.[46] The geometry is a 5° half-angle axisymmetric blunt cone 1 meter in length with a nose radius of 1 mm. The DNS used 256 points in the wall-normal direction and roughly 10 points/mm on the surface of the cone in the streamwise direction. In the azimuthal direction, a Fourier collocation method is used with four points. LST simulations interpolated the DNS mean flow onto the LST grid stretching methods discussed in Sec. IV B. As will be explained in Secs. III and IV, the DNS code used in this study utilizes a shock-fitting method. Thus, the parameters in Table I are the free stream conditions upstream of the shock formed over the body.

III. GOVERNING EQUATIONS AND GAS MODEL

The governing equations for the DNS and LST codes are those developed by Mortensen and Zhong,[48–53] which are formulated for thermochemical nonequilibrium assuming a two-temperature model. Their formulation is highlighted here for clarity. The rotational energy mode is assumed to be fully excited with up to eleven non-ionizing species with finite-rate chemistry. Two-temperatures are used to represent translation-rotation energy and vibration energy, and a five-species model (N_2, O_2, NO, N, and O) is used here to simulate air. The Navier-Stokes equations in conservative form consist of five species mass conservation equations, three momentum conservation equations, the total energy equation, and the vibration energy equation. The governing equations in vector form are written as

$$\frac{\partial U}{\partial t} + \frac{\partial F_j}{\partial x_j} + \frac{\partial G_j}{\partial x_j} = W, \tag{5}$$

where U is the state vector of conserved quantities, W is the source terms, and F_j and G_j are the inviscid and viscous flux vectors, respectively. For further details of the governing equations and thermochemical model, see the work of Knisely and Zhong[43,46] and Mortensen.[53]

IV. NUMERICAL METHODS

A. DNS

In order to perform a stability analysis using LST, a steady mean flow from DNS must be obtained. Here, only a brief overview of the DNS numerical methods is given, with additional details in Paper II.[65] The thermochemical nonequilibrium code developed by Mortensen and Zhong[48–53] utilizes a high-order shock-fitting method to compute the flow field between the shock and the body. For shock-fitting computations, the shock location is not known *a priori*, so its position is solved along with the flow field. Since the shock position is not stationary, the grid used to compute the flow field is a function of time. A seven point stencil is used to discretize the spatial derivatives, resulting in a low dissipation fifth order upwinded difference for the inviscid terms and a central scheme for the viscous terms. The derivatives in the transverse direction, if required, are treated with Fourier collocation. To compute second derivatives, the first order derivative operator is applied twice. A low storage 1st-order Runge-Kutta method from Williamson[54] is used to advance the solution in time. Conditions behind the shock are calculated from Rankine-Hugoniot relations. In the free stream, the flow is assumed to be in thermal equilibrium and the chemical composition of the flow is frozen. The shock is assumed to be infinitely thin with all relaxation occurring downstream due to finite relaxation rates. This leads to the chemical composition remaining constant across the shock, as well as the vibration temperature.

B. LST

The linear stability analysis used here is largely based on the LST code developed by Mortensen;[53] however, here the assumption of zero wall-normal velocity is relaxed (i.e., $\bar{v} \neq 0$), and new free stream boundary conditions incorporating a shock at the computational boundary are used. Curvature in the streamwise and transverse directions is included similar to Malik and Spall,[55] with further details in Appendix A. The LST equations are derived from the governing equations [Eq. (5)], where the instantaneous flow is comprised of mean and fluctuating components, where the mean flow is assumed to satisfy the governing equations and is subtracted out. The mean flow is assumed to be a function of y only and the flow disturbances are assumed to be small, i.e., linear. The perturbations are then assumed to be in the form of a normal mode described by $q' = \hat{q}(y)\exp[i(\alpha x + \beta z - \omega t)]$, where ω is the circular frequency of the disturbance and α and β are the wavenumbers. For comparison to direct numerical simulation, the spatial stability approach is used, i.e., α is complex which results in the dispersion relation $\alpha = \Omega(\omega, \beta)$.

Substituting in the normal mode form for the perturbation reduces the problem for a species model with ns species to a coupled set of $ns + 5$ ordinary differential equations

$$\left(\mathbf{A}\frac{d^2}{dy^2} + \mathbf{B}\frac{d}{dy} + \mathbf{C}\right)\vec{\phi} = \vec{0}, \tag{6}$$

where $\vec{\phi} = \left[\hat{\rho}_1, \hat{\rho}_2, \ldots, \hat{\rho}_{ns}, \hat{u}, \hat{v}, \hat{w}, \hat{T}, \hat{T}_V\right]^T$ and **A**, **B**, and **C** are complex square matrices of size $ns + 5$ and are included in Appendix A. This is now a boundary value problem where the derivative operators can be discretized and the equations solved numerically.

For hypersonic compressible boundary layers, it is important to have high grid resolution near the generalized inflection point.[4] The grid used by Mortensen[53] uses two different functions to cluster points around the inflection point and near the wall. It is called the cosine-exponential grid. In hypersonic flows in which the spontaneous radiation of sound occurs, the cosine-exponential grid may not provide enough grid resolution in the free stream or near the outer shock boundary. The continuous modes oscillate to the computational boundary in many cases. Therefore, it is helpful to use an additional exponential grid stretching function at the edge of the computational boundary used by Knisely and Zhong.[46]

With the grid defined, Eq. (6) can be transformed into computational space and a numerical representation of the derivatives can be given. The first and second derivative operators in the wall-normal direction are discretized by taking derivatives of Lagrange polynomials in physical space. Mortensen's[53] scheme can be applied for variable stencil sizes and can be used to obtain high-order approximations. Here, a five-point stencil is used, resulting in a 4th order method similar to the one used by Malik.[15]

After discretization, nonlinearities exist in α so the global method suggested by Malik[15] is used to compute the eigenvalue spectrum with $\alpha^2 = 0$. This method computes the eigenvalues from a generalized eigenvalue problem $\tilde{A}\vec{\phi} = \alpha\tilde{B}\vec{\phi}$, where the LAPACK[56] subroutine ZGGEV is used here for solution. From the eigenvalue spectrum, an initial guess can be obtained for the local method which results in $\bar{A}\vec{\phi} = \bar{B}$ and the eigenvalue is found iteratively without dropping the α^2 terms. This iterative method of solution requires the velocity perturbation at the wall $\hat{u}(0)$ be treated as a free parameter and be iteratively driven to zero within a small tolerance. The LAPACK subroutine ZGESV is used to solve the local problem. It is also possible to avoid the computationally intensive global method and obtain an initial guess for α from a nearby streamwise location or a DNS assuming the unsteady DNS results are available.

To estimate boundary-layer transition using LST, the e^N transition criterion is used which is defined as

$$e^N = \frac{A(s)}{A_0} = \exp\left[\int_{s_0}^{s} -\alpha_i(s,f)ds\right], \tag{7}$$

where $A(s)$ is the integrated disturbance amplitude, A_0 is the initial disturbance amplitude, s_0 is the location where the disturbance first becomes unstable, and α_i is the spatial amplification rate obtained from LST. In-flight transition N-factors are commonly understood to be around 10. Malik[23] showed that 9.5 and 11.2 correlated with transition onset for two high Mach number flight tests. In ground-based experimental test facilities, the transition N-factor is usually lower.

1. New LST shock boundary conditions

Boundary conditions to solve the LST problem are required at the wall and in the free stream. There are $ns + 5$ independent variables in LST, and therefore $ns + 5$ conditions are needed at the free stream boundary, with $ns + 4$ conditions specified at the wall due to the iteration on $\hat{u}(0)$ discussed previously. At the wall, a high-order pressure extrapolation condition assuming zero mass flux from the wall and zero temperature perturbation are used

$$\frac{d\hat{p}}{dy} = 0, \qquad \hat{v} = \hat{w} = \hat{T} = \hat{T}_V = 0, \tag{8}$$

although more complex ablation boundary conditions can be used.[53] In the free stream, in flows in which the supersonic modes are not a concern, all perturbations except $\hat{v}$ at the outer edge can simply be set to zero, and the $\hat{v}$ boundary condition is obtained from the continuity equation. When this is the case, the free stream boundary conditions are

$$\bar{\rho}\frac{d\hat{v}}{dy} + \frac{d\bar{\rho}}{dy}\hat{v} = 0, \qquad \hat{\rho}_s = \hat{u} = \hat{w} = \hat{T} = \hat{T}_V = 0. \tag{9}$$

However, in flows with supersonic modes, there is highly oscillatory eigenfunction behavior in the free stream. Using these zero-boundary conditions may not be physically relevant in this situation, especially when the boundary coincides with a shock. Therefore, free stream boundary conditions based on the Rankine-Hugoniot relations with a free shock approximation were derived, following similar methods to Chang *et al.*[29,57]

The LST shock boundary conditions make the same assumptions as the DNS shock-fitting scheme. The flow upstream of the shock is assumed to be in thermal equilibrium with a fixed chemical composition. The shock is assumed to be infinitely thin, resulting in no relaxation across the shock. In other words, there is no change in chemical composition or vibrational temperature across the shock. The flow surrounding the shock is assumed to be inviscid. Under these conditions, the governing equations in conservative form can be rewritten as

$$\frac{\partial U}{\partial t} + \frac{\partial F_j}{\partial x_j} = 0, \tag{10}$$

where

$$U = \begin{bmatrix} \rho_1 \\ \vdots \\ \rho_{ns} \\ \rho u_1 \\ \rho u_2 \\ \rho u_3 \\ \rho e \\ \rho e_v \end{bmatrix}, \quad \frac{\partial F_j}{\partial x_j} = \frac{\partial}{\partial x_j} \begin{bmatrix} \rho_1 u_j + \rho_1 u_{1j} \\ \vdots \\ \rho_{ns} u_j + \rho_1 u_{nsj} \\ \rho u_1 u_j + p\delta_{1j} \\ \rho u_2 u_j + p\delta_{2j} \\ \rho u_3 u_j + p\delta_{3j} \\ (p + \rho e) u_j \\ \rho e_v u_j \end{bmatrix} = \frac{\partial E}{\partial x} + \frac{\partial F}{\partial y} + \frac{\partial G}{\partial z}, \tag{11}$$

where it can be shown $u_{si} = D_s\left(c_s \frac{\partial \rho}{\partial x_i} - \frac{\partial \rho_s}{\partial x_i}\right)$. Equation (10) is transformed into a coordinate system of the shock, illustrated in Fig. 4.

The position of the shock in Cartesian coordinates is $y_s = f(x, z, t)$, with the mean shock position $\overline{y_s} = \bar{f}(x)$. Thus the local slope of the shock can be written as $a = \tan\theta = \frac{d\bar{f}}{dx}$. The transformation between (x, y, z) and (ξ, η) is

$$\xi = \frac{x}{b}, \tag{12}$$

$$\eta = b[y - f(x, z, t)], \tag{13}$$

where $b = \cos\theta$.

Under this transformation, Eq. (10) becomes

$$\frac{\partial f}{\partial t}\frac{\partial U}{\partial \eta} - \frac{1}{b^2}\frac{\partial E}{\partial \eta} + \frac{\partial f}{\partial x}\frac{\partial E}{\partial \eta} - \frac{\partial F}{\partial \eta} + \frac{\partial f}{\partial z}\frac{\partial G}{\partial \eta} = 0. \tag{14}$$

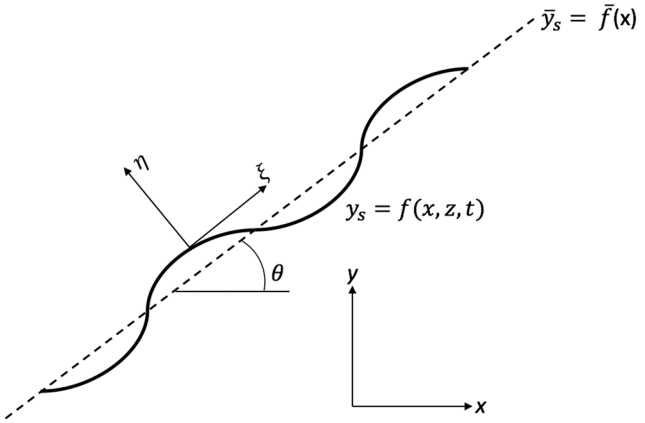

FIG. 4. Schematic of the unsteady position of a shock in (ξ, η) and (x, y, z) coordinate systems.

Integrating Eq. (14) from $\eta = -\epsilon$ to $\eta = \epsilon$ and taking the limit as $\epsilon \to 0$ result in

$$\frac{\partial f}{\partial t}\Delta U + \frac{\partial f}{\partial x}\Delta E - \Delta F + \frac{\partial f}{\partial z}\Delta G = 0, \tag{15}$$

where the Δ terms are the jump conditions across the shock. For example, $\Delta U = U_\infty - U_{shock}$ where the subscript ∞ denotes the conditions immediately upstream of the shock and *shock* denotes conditions immediately downstream of the shock. All flow variables, including f, are perturbed and linearized such that $\phi = \overline{\phi} + \phi'$. Assuming the perturbed variables behave as a normal mode, $\phi' = \hat{\phi}(y)e^{i(\alpha x + \beta z - \omega t)}$ results in

$$\hat{f}\left(-i\omega\Delta\overline{U} + i\alpha\Delta\overline{E} + i\beta\Delta\overline{G}\right) + a\Delta E' - \Delta F' = 0, \tag{16}$$

where

$$\Delta E' = \begin{bmatrix} \overline{\rho_1}\hat{u} + \hat{\rho_1}\overline{u} + \overline{D_1}\left(\overline{c_1} i\alpha \sum_{s=1}^{ns} \hat{\rho}_s - i\alpha\hat{\rho}_1\right) \\ \vdots \\ \overline{\rho_{ns}}\hat{u} + \hat{\rho_{ns}}\overline{u} + \overline{D_{ns}}\left(\overline{c_{ns}} i\alpha \sum_{s=1}^{ns} \hat{\rho}_s - i\alpha\hat{\rho}_{ns}\right) \\ \hat{\rho}\overline{u}^2 + 2\overline{\rho u}\hat{u} + \hat{p} \\ \hat{\rho}\overline{u}\overline{v} + \overline{\rho v}\hat{u} + \overline{\rho u}\hat{v} \\ \hat{\rho}\overline{u}\overline{w} + \overline{\rho w}\hat{u} + \overline{\rho u}\hat{w} \\ \hat{u}(\overline{\rho e} + \overline{p}) + \overline{u}(\hat{\rho e} + \hat{p}) \\ \overline{\rho e_v}\hat{u} + \rho\hat{e}_v\overline{u} \end{bmatrix}, \quad \Delta F' = \begin{bmatrix} \overline{\rho_1}\hat{v} + \hat{\rho_1}\overline{v} \\ \vdots \\ \overline{\rho_{ns}}\hat{v} + \hat{\rho_{ns}}\overline{v} \\ \hat{\rho}\overline{u}\overline{v} + \overline{\rho v}\hat{u} + \overline{\rho u}\hat{v} \\ \hat{\rho}\overline{v}^2 + 2\overline{\rho v}\hat{v} + \hat{p} \\ \hat{\rho}\overline{v}\overline{w} + \overline{\rho w}\hat{v} + \overline{\rho v}\hat{w} \\ \hat{v}(\overline{\rho e} + \overline{p}) + \overline{v}(\hat{\rho e} + \hat{p}) \\ \overline{\rho e_v}\hat{v} + \rho\hat{e}_v\overline{v} \end{bmatrix}. \tag{17}$$

Linearizing the Rankine-Hugoniot relations introduces an extra perturbation variable for the shock position, $\hat{f}$. To eliminate the extra variable, $\hat{f}$ is solved for in terms of the other perturbation variables using the x-momentum equation. However, this reduces the system to $ns + 4$ equations for $ns + 5$ independent perturbation variables. The $ns + 4$ equations can

be represented by

$$\sum_{j=1}^{ns+5} \hat{B}_{ij}\hat{\phi}_j = 0, \quad i = 1, 2, \ldots, ns+4, \tag{18}$$

where the terms in $\hat{B}$ are included in Appendix B.

To close the system of equations for the shock boundary conditions, an extra equation is needed, for which there are a number of options. The first considered uses the mixture continuity equation, which, when set into the LST framework becomes

$$\overline{v}\frac{d\hat{\rho}}{dy} + \hat{\rho}\left(-i\omega + i\alpha + \frac{d\overline{v}}{dy}\right) + i\alpha\overline{\rho}\hat{u} + \overline{\rho}\frac{d\hat{v}}{dy} + \frac{d\overline{\rho}}{dy}\hat{v} + i\beta\overline{\rho}\hat{w} = 0. \tag{19}$$

The second closure equation considered was the y-momentum equation, which has already been put into the LST framework and is contained in the matrices **A**, **B**, and **C** in Appendix A.

The third closure equation used was the right-running characteristic equation derived from the 2D Euler equations for a perfect gas. Transforming to the LST framework, the characteristic equation becomes

$$\begin{aligned}
&\sum_{s=1}^{ns}\left[-i\omega\frac{\mathcal{R}}{M_s}\overline{T} + i\alpha\mathcal{R}\overline{T}\left(k_x\overline{u} + k_y\overline{v} + \overline{c}\right) + \frac{\mathcal{R}}{M_s}\frac{d\overline{T}}{dy} + \overline{c}\left(k_x\frac{d\overline{u}}{dy} + k_y\frac{d\overline{v}}{dy}\right)\right]\hat{\rho}_s + \overline{\rho}\overline{c}k_x\left[-i\omega + i\alpha\left(k_x\overline{u} + k_y\overline{v} + \overline{c}\right) + k_x\frac{d\overline{u}}{dy} + k_y\frac{d\overline{v}}{dy}\right]\hat{u} \\
&+ \overline{\rho}\overline{c}k_y\left[-i\omega + i\alpha\left(k_x\overline{u} + k_y\overline{v} + \overline{c}\right) + k_x\frac{d\overline{u}}{dy} + k_y\frac{d\overline{v}}{dy}\right]\hat{v} + \overline{\rho}\left[-i\omega\mathcal{R} + i\alpha\mathcal{R}\left(k_x\overline{u} + k_y\overline{v} + \overline{c}\right) + \frac{\mathcal{R}}{\overline{\rho}}\frac{d\overline{\rho}}{dy}\right] \\
&+ \frac{1}{2}\frac{\overline{c}}{\overline{T}}\left(k_x\frac{d\overline{u}}{dy} + k_y\frac{d\overline{v}}{dy}\right)(1 + \overline{\rho}\overline{c})\Big]\hat{T} + \sum_{s=1}^{ns}\frac{\mathcal{R}}{M_s}\overline{T}\frac{d\hat{\rho}_s}{dy} + k_x\overline{\rho}\overline{c}\left(k_x\overline{u} + k_y\overline{v} + \overline{c}\right)\frac{d\hat{u}}{dy} + k_y\overline{\rho}\overline{c}\left(k_x\overline{u} + k_y\overline{v} + \overline{c}\right)\frac{d\hat{v}}{dy} + \overline{\rho}\mathcal{R}\frac{d\hat{T}}{dy} = 0,
\end{aligned} \tag{20}$$

where $u^* = uk_x + vk_y$, k_x and k_y are unit vectors in the x and y directions, respectively, and c is the local speed of sound.

As will be shown in verifying these closure schemes for the LST shock boundary condition, there were only minimal differences in results depending on which the closure equation was used. However since the y-momentum equation was already cast into the LST framework and hard-coded into the LST program, it was the simplest closure equation to implement yet also produced the smoothest solution near the shock. Therefore, the y-momentum equation was used as the shock boundary condition closure equation.

V. STEADY FLOW FIELD SOLUTION

In the nose region of the cone for both cases, there is significant chemical and thermal nonequilibrium. Farther downstream, however, the chemical nonequilibrium effects weaken.

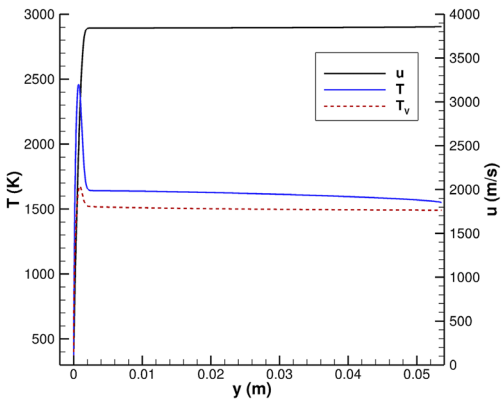

(a)

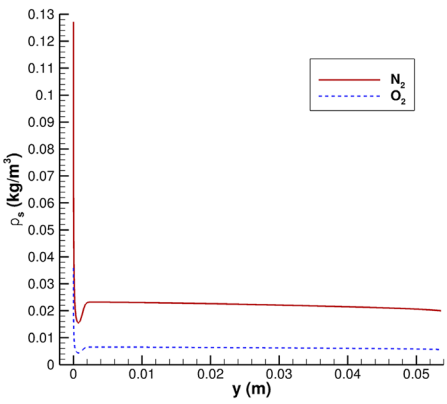

(b)

FIG. 5. Case 1 mean flow boundary layer profiles at s = 0.4 m. (a) u, T, and T_V. (b) Species density ρ_s of N_2 and O_2 species. u denotes the component of velocity tangential to the surface of the cone. y is the wall normal distance.

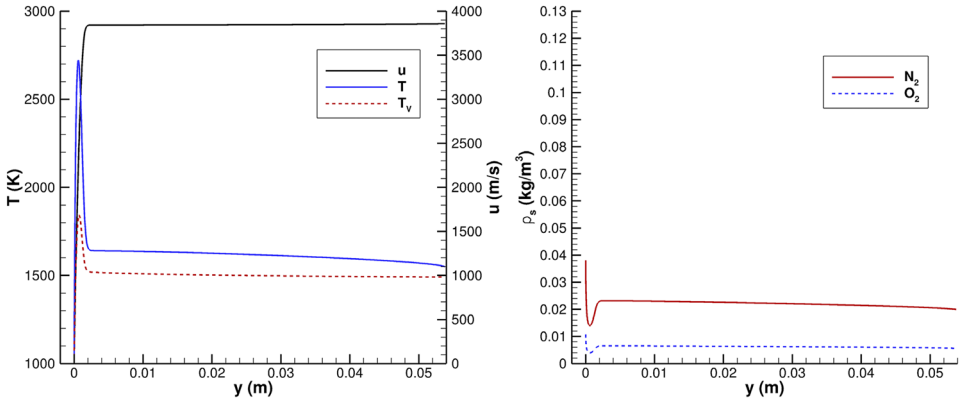

FIG. 6. Case 2 mean flow boundary layer profiles at s = 0.4 m. (a) u, T, and T_V. (b) Species density ρ_s of N_2 and O_2 species. u denotes the component of velocity tangential to the surface of the cone. y is the wall normal distance.

Boundary layer profiles for temperature, vibration temperature, tangential velocity, and species density of N_2 and O_2 at a streamwise distance from the stagnation point of s = 0.4 m are shown in Fig. 5 for case 1 and Fig. 6 for case 2. Hereafter, y denotes the wall-normal distance. Due to the cold wall, the boundary layer is thin in relation to the flow domain in both cases. The mean flow does not reach thermal equilibrium in the free stream, thus demonstrating the necessity of accounting for nonequilibrium effects in these types of flows. The species densities of N_2 and O_2 are nearly identical in the free stream between cases 1 and 2, however, due to the colder wall in case 1, the air is denser and there is a very steep density gradient near the wall.

VI. LST VERIFICATION

The steady DNS results were used to obtain stability predictions using LST. Before presenting results from the LST analysis, however, the modifications to the LST code must be verified. This was accomplished by comparing the new LST code with the LST code developed by Mortensen,[53] which has already been successfully verified against Hudson's[58] code. The test case is a supersonic mode at s = 0.73 m at a frequency of f = 550 kHz in case 1.

A. Nonparallel meanflow

First, the assumption of $\bar{v} = 0$ made in the previous iterations of the LST code by Mortensen[53] is relaxed. For traditional modes whose eigenfunctions decay rapidly outside the boundary layer, the assumption of $\bar{v} = 0$ is suitable. However, far outside the boundary layer, the magnitude of $\bar{v}$ may become non-negligible and may have an impact on the eigenfunction behavior of the supersonic mode in the free stream.

Because the original LST code with $\bar{v} = 0$ has already been verified,[53] this previous version of the code is used as a benchmark for the new code with $\bar{v} \neq 0$. The eigenvalues and eigenfunctions for f = 550 kHz at s = 0.73 m using 1500 LST points are used as the test case. The initial comparison between $\bar{v} = 0$ and $\bar{v} \neq 0$ utilize the Dirichlet (zero) free stream boundary condition. This particular location and frequency was chosen because it represents the supersonic continuous mode F1$^+$. The comparison of the eigenvalues of the two codes is summarized in Table II. Relaxing the $\bar{v} = 0$ assumption results in very small differences in α_r and therefore c_r (approximately 0.02% difference); however, there is a considerable difference in growth rate $-\alpha_i$. The growth rate increases by about 27.6%, which can cause a significant difference in transition prediction calculations such as the e^N method.

The mode shapes of the pressure eigenfunction are also compared between the $\bar{v} = 0$ and $\bar{v} \neq 0$ codes. The whole domain is shown in Fig. 7(a), and the outer edge region is shown in detail in 7(b). From Fig. 7(a), there is a clear difference in the magnitude of the pressure eigenfunction, $|p|$, in the center region of the domain from about y = 0.01 m and y = 0.07 m. The $\bar{v} \neq 0$ code predicts a slightly smaller amplitude in the pressure eigenfunction in this region. Within the boundary layer ($y < 0.01$ m), however, the $\bar{v} \neq 0$ results are in agreement with the $\bar{v} = 0$ results. At the outer edge of the computational domain, the amplitude of the pressure eigenfunction is smaller for $\bar{v} \neq 0$. Additionally, it appears that the two codes are slightly out of phase with one another, although the magnitudes are quite small in relation to the magnitudes in the boundary layer.

TABLE II. Comparison of eigenvalues between LST codes with $\bar{v} = 0$ and $\bar{v} \neq 0$. f = 550 kHz, s = 0.73 m, and 1500 LST points. Nondimensional phase speed $c_r = (\omega^*/u^*_\infty)/\sqrt{\beta^2 + \alpha_r^2}$, where $\omega^* = 2\pi f$ is the dimensional circular frequency and u^*_∞ is the free stream velocity upstream of the shock.

	Mode F1$^+$ values		
	α_r (m^{-1})	$-\alpha_i$ (m^{-1})	c_r
$\bar{v} = 0$	1240.6008	5.307 05	0.717 476
$\bar{v} \neq 0$	1240.2478	6.772 75	0.717 681

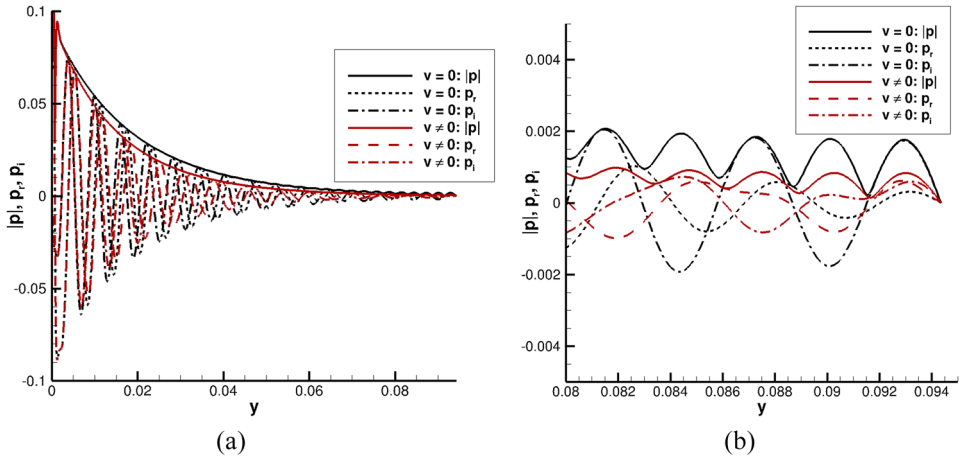

FIG. 7. Comparison of the pressure eigenfunction for $\bar{v} = 0$ and $\bar{v} \neq 0$. f = 550 kHz, s = 0.73 m, and 1500 LST points. (a) Whole domain and (b) outer edge region.

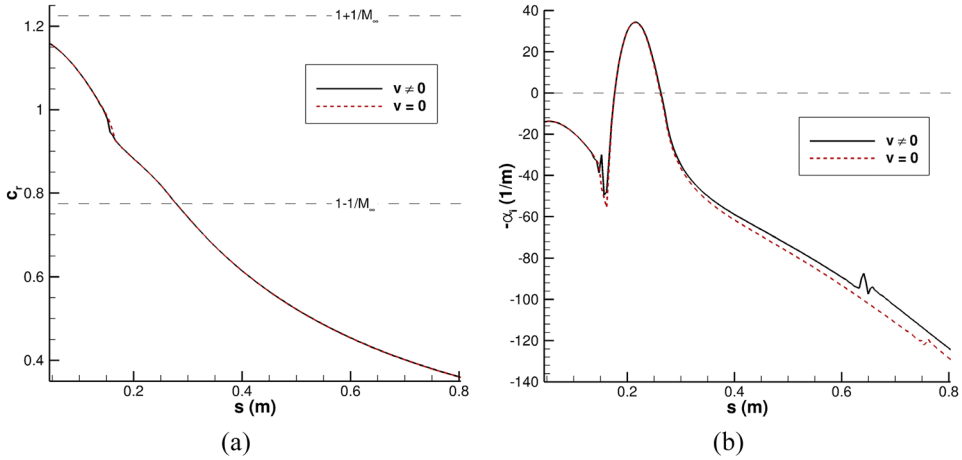

FIG. 8. Comparison of (a) phase speed and (b) growth rate for $\bar{v} = 0$ and $\bar{v} \neq 0$, f = 1 MHz. M_∞ = 4.44 is the mean flow Mach number immediately downstream of the shock.

Finally, the growth rate and phase speed for each streamwise location are compared for the $\bar{v} = 0$ and $\bar{v} \neq 0$ assumptions. For a fixed frequency of f = 1 MHz, shown in Fig. 8, the phase speed between $\bar{v} = 0$ and $\bar{v} \neq 0$ is virtually indistinguishable. Note near s = 0.15 m the small oscillations in growth rate and jump in phase speed. This phenomenon is due to the synchronization of mode F1 with the entropy/vorticity spectra.[59] The growth rate agreement between $\bar{v} = 0$ and $\bar{v} \neq 0$ is quite good upstream; however, $\bar{v} \neq 0$ begins to deviate for s > 0.3 m. This area of disagreement corresponds to the region in which $c_r < 1 - 1/M_\infty$, where M_∞ = 4.44 is taken hereafter in the LST analysis as the Mach number immediately downstream of the shock, which is the region of interest for supersonic modes. Therefore, it is important to include $\bar{v} \neq 0$ in the LST analysis.

B. LST shock boundary conditions

As evidenced in Fig. 7(a), the eigenfunctions of the supersonic mode can be significantly oscillatory outside of the boundary layer. In order to determine whether or not the Dirichlet (zero) boundary conditions are appropriate in this situation, the shock boundary conditions are implemented and compared. Additionally, the impact of the closure equation for the shock boundary conditions is explored.

TABLE III. Comparison of eigenvalues between Dirichlet (zero) boundary conditions and shock boundary conditions for each closure equation. f = 550 kHz, s = 0.73 m, and 1500 LST points. Nondimensional phase speed $c_r = (\omega^*/u^*_\infty)/\sqrt{\beta^2 + \alpha_r^2}$, where $\omega* = 2\pi f$ is the dimensional circular frequency and u^*_∞ is the free stream velocity upstream of the shock.

	Mode F1⁺ values		
Closure equation	α_r (m^{-1})	$-\alpha_i$ (m^{-1})	c_r
Zero	1240.2478	6.772 757	0.717 681
Continuity	1240.2478	6.772 861	0.717 681
y-momentum	1240.2478	6.772 866	0.717 681
Characteristic	1240.2478	6.772 906	0.717 681

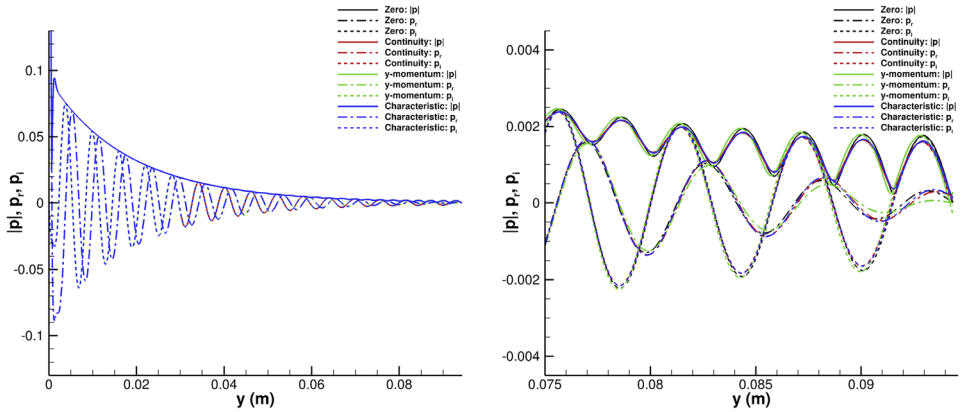

FIG. 9. Comparison of the pressure eigenfunction for Dirichlet (zero) boundary conditions and shock boundary conditions for each closure equation. f = 550 kHz, s = 0.73 m, and 1500 LST points. (a) Whole domain and (b) outer edge region.

The test case is again the supersonic continuous mode F1$^+$ from the mean flow from case 1 at f = 550 kHz and s = 0.73 m using 1500 LST points. The difference in eigenvalues between the zero boundary conditions and between each closure equation is summarized in Table III, while the pressure eigenfunctions are compared in Fig. 9. The whole domain is shown in Fig. 9(a), and the edge of the computational domain is enlarged in Fig. 9(b). There is no difference within computational accuracy in this particular case between the zero and shock boundary condition eigenvalues or eigenfunctions. This is likely due to the computational domain being very large with respect to the boundary layer. For locations further upstream, this may not be the case and the shock boundary conditions may be more critical. However, because the shock boundary conditions do not add any additional computational cost and are more physically relevant to the flow, they are used instead of the zero boundary conditions. Between each shock boundary condition closure equation, there is minimal difference. The y-momentum closure equation converged the quickest of the three equations and is therefore used in future computations.

VII. NUMERICAL ACCURACY

A. Steady flow field solution grid independence

The steady flow field grid points in the wall-normal direction for case 1 were doubled to 512 points from 256 to determine the number of grid points required for a grid-independent solution. The wall-normal grid density is known to be much more critical than the wall-tangent grid density. Mean flow boundary layer profiles at s = 0.4 m (Fig. 10) indicate very little difference in the mean flow profiles when the grid is doubled. Furthermore, doubling the grid for the steady flow field solution significantly increased the computational expense to obtain a converged solution. Therefore, 256 grid points in the wall-normal direction were sufficient to provide an accurate solution.

B. LST grid independence

The number of grid points in the LST simulation was varied between 500 and 1500 points in the wall-normal direction to determine the number of grid points to obtain a

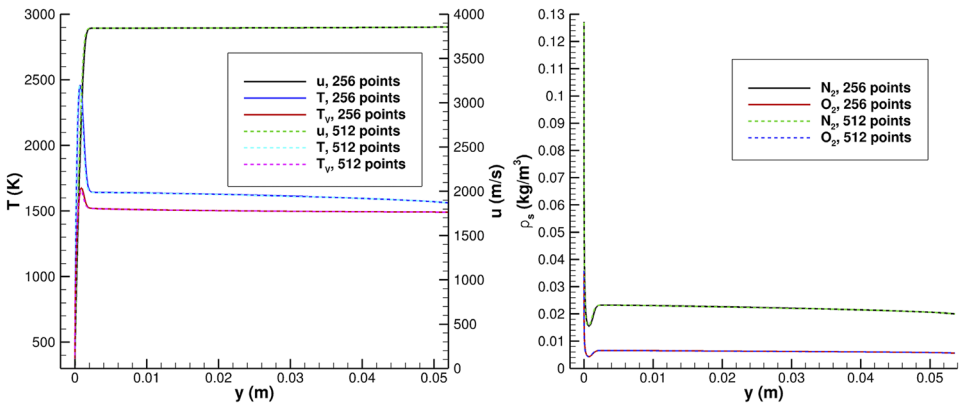

FIG. 10. Wall-normal grid point comparison of case 1 mean flow boundary layer profiles at s = 0.4 m. (a) u, T, and T_V. (b) Species density ρ_s of N_2 and O_2 species.

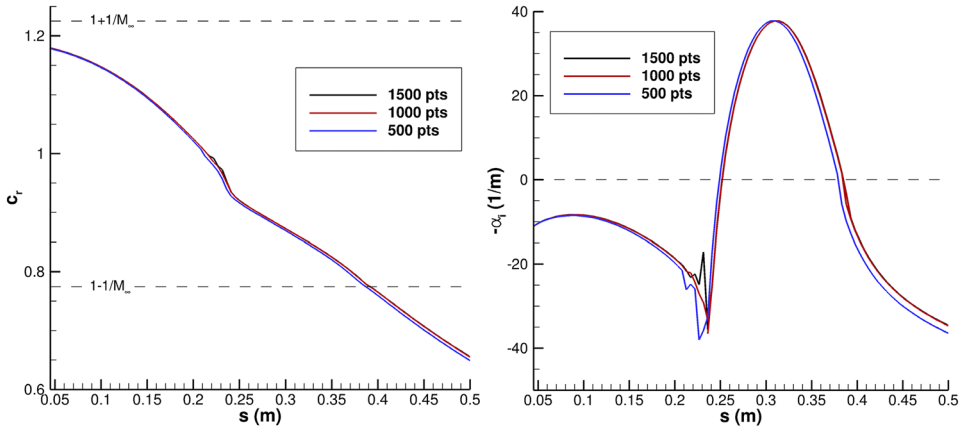

FIG. 11. Comparison of (a) phase speed, c_r, and (b) growth rate, $-\alpha_i$, for case 1 mode F1 at f = 800 kHz with 500, 1000, and 1500 LST grid points. M_∞ = 4.44 is the mean flow Mach number immediately downstream of the shock.

grid-independent solution. The 800 kHz mode F1 from case 1 was used as the benchmark for the grid refinement study, as shown in Fig. 11. There are small differences in both phase speed and growth rate for 500 grid points compared to the 1500 point case. The 1000 grid point case and the 1500 grid point case are nearly identical, indicating that 1000 grid points are sufficient. However, to err on the side of caution, 1500 grid points are used in the LST calculations. Furthermore, increasing the number of grid points in LST did not increase the computational time severely.

VIII. LST RESULTS

LST was performed to determine which modes were unstable. All LST calculations performed here assume a spanwise wavenumber of β = 0. As previously stated, 1500 wall-normal grid points were used, and the shock free stream boundary condition with the y-momentum closure equation was used. The global method, which assumes α^2 = 0, was used at a fixed streamwise location and frequency to obtain an initial guess for the eigenvalues of the physical modes. The local method, which does not neglect α^2, then used this initial guess and iterated to a converged solution. Once the eigenvalues of a physical mode have been obtained, it is possible to march in the streamwise direction using the eigenvalues from the previous location as an initial guess. At each streamwise location, the spatial growth rate is given by the negative of the imaginary component of the eigenvalue ($-\alpha_i$), and the phase speed is calculated from the real component of α. The nondimensional phase speed is defined as $c_r = \frac{(\omega^*/u^*_\infty)}{\sqrt{\beta^2+\alpha_r^2}}$, where $\omega* = 2\pi f$ is the dimensional circular frequency and u^*_∞ is the free stream velocity upstream of the shock.

A. Case 1 LST results

A phase speed and growth rate plot in the style of Ma and Zhong[14] is shown for case 1 in Fig. 12 for a frequency of f = 1 MHz. Following similar notation as Fedorov[60] discussed in the introduction, the results in Fig. 12 indicate that mode F1

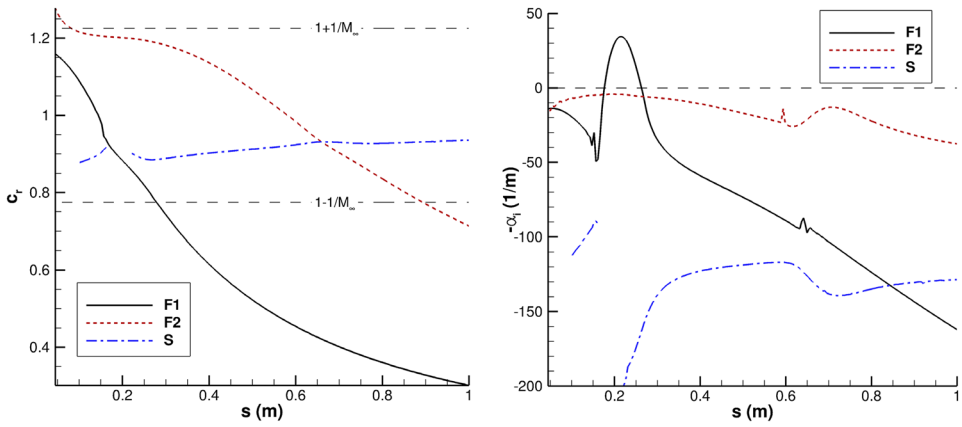

FIG. 12. Case 1 LST phase speed and growth rate for modes F1, F2, and S at f = 1 MHz. (a) Phase speed and (b) growth rate. M_∞ = 4.44 is the mean flow Mach number immediately downstream of the shock.

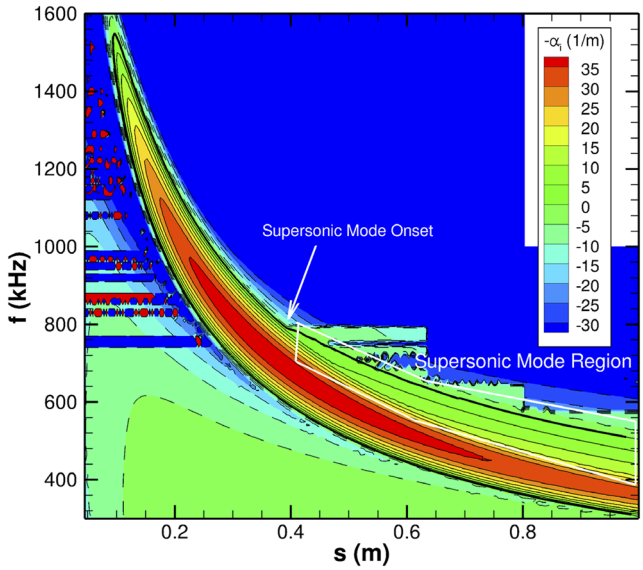

FIG. 13. Case 1 neutral stability map for second mode. Dashed lines indicate negative growth rates. The thick black line indicates points of neutral stability. The white arrow indicates the onset of supersonic mode. The white box indicates the region of supersonic mode.

becomes unstable, while mode S is stable. Again, it is conventional to describe the unstable mode as "Mack's second mode," even though mode S is stable here. Therefore, all references to the second mode hereafter indicate the mode F1 instability. Mode F1 becoming the dominant instability is consistent with Bitter and Shepherd.[26] It should be noted that the discontinuity in mode S in Fig. 12 (and in Figs. 14, 19, and 20) is due to the LST solver having difficulty resolving the synchronization region of two discrete modes. Due to the iterative method of solution, the weaker discrete mode is more difficult to capture. Furthermore, as Fedorov and Tumin[5] noted, the synchronization of the two discrete modes actually creates a singularity in the LST framework and causes difficulties in traditional stability methods.

The streamwise marching procedure was repeated for a number of frequencies, producing the neutral stability map for the second mode in Fig. 13, indicating the locations and frequencies in which a disturbance grows. Neutrally stable points ($-\alpha_i = 0$) are shown as the thick black line. All points inside of the curve formed by the neutral points have positive growth rates. At frequencies below roughly f = 800 kHz, and streamwise distances greater than s = 0.4, the upper branch of the neutral curve broadens, indicating the presence of the supersonic mode. The onset of the supersonic mode coincides with the "kink" in the upper branch of the neutral curve, indicated by the white arrow in Fig. 13. Bitter and Shepherd[26] noted that the unstable supersonic modes increase the range of instability; therefore, this particular region on the neutral stability curve indicated by the white box in Fig. 13 was examined in finer detail through growth rate and phase speed plots for individual frequencies.

Supersonic unstable modes were found for frequencies below f = 800 kHz. The growth rate and phase speed plots for a number of unstable supersonic modes are shown in Fig. 14. The effect of mode S and mode F1 synchronizing can be seen in the "bending" and "jumping" of the phase speeds of the modes.[5] Similar to Bitter and Shepherd,[26] mode F1 bifurcates into two distinct modes upon synchronization with the slow acoustic spectrum, indicated by the kink in the growth rate curves. Following similar notation to Bitter and Shepherd[26] and Fedorov and Tumin,[5] the unstable mode is denoted as $F1^+$, and the new stable mode as $F1^-$. Synchronization with the slow acoustic spectrum causes mode $F1^+$ to change from a discrete mode to a continuous mode and simultaneously creates the discrete mode $F1^-$. The major difference between discrete and continuous modes is the behavior of the eigenfunctions in the free stream. Discrete modes have eigenfunctions which decay in amplitude outside of the boundary layer, whereas

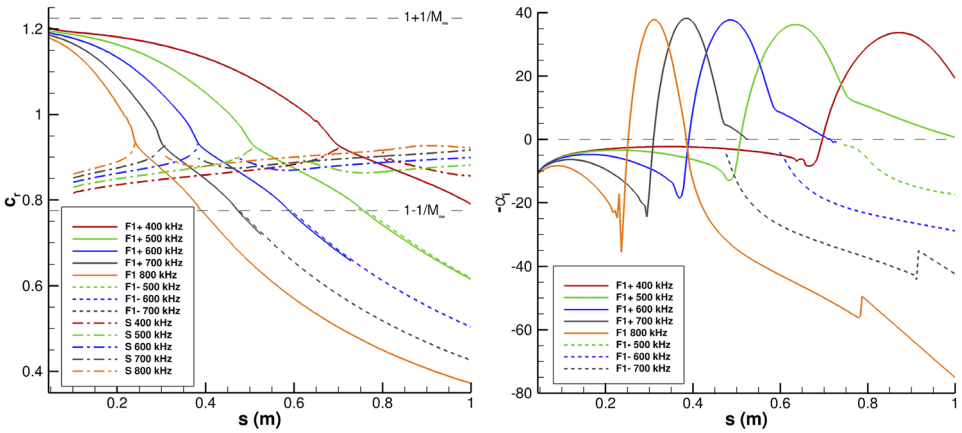

FIG. 14. Case 1 LST phase speed and growth rate for supersonic unstable modes. (a) Phase speed and (b) growth rate. Dashed lines indicate the new modes created by synchronization with the slow acoustic spectrum. M_∞ = 4.44 is the mean flow Mach number immediately downstream of the shock.

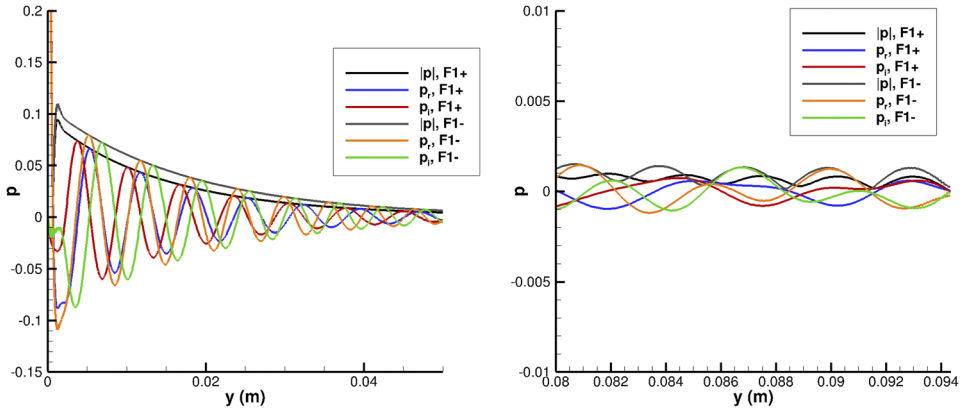

FIG. 15. Case 1 pressure eigenfunction normalized by local pressure for unstable and stable supersonic mode branches at f = 550 kHz and s = 0.73 m. Phase speed and growth rate for mode F1$^+$: c_r = 0.717, $-\alpha_i$ = 5.33 m^{-1}. Mode F1$^-$: c_r = 0.728, $-\alpha_i$ = −10.59 m^{-1}. (a) Highly oscillatory boundary layer region and (b) weakly oscillatory region near the shock.

continuous modes have oscillatory behavior in the free stream. From Fig. 14, mode F1$^+$ (solid line) remains unstable for longer along the streamwise distance, which may lead to transition earlier on the body. After becoming stable, mode F1$^+$ ceases to exist and merges with the slow acoustic continuous spectrum, as it does in results presented by Bitter and Shepherd.[26] Mode F1$^-$ (dotted line) becomes increasingly stable downstream but exhibits a similar eigenfunction to mode F1$^+$ at first, as shown in Fig. 15 for f = 550 kHz at s = 0.73 m. The pressure eigenfunction is scaled by local flow values and is equal to unity at the wall. The axis limits for the eigenfunctions shown in Fig. 15 are modified to show details in each oscillatory region. For both the unstable and stable modes, the fluctuations in the eigenfunctions extend well into the free stream, similar to results presented by Bitter and Shepherd.[26]

In visualizing the merging of mode F1$^+$ with the slow acoustic continuous spectrum, it is instructive to examine the dispersion relation shown in Fig. 16. The data are exactly the same as in Fig. 14; however, the dispersion relation shows the relationship between the phase speed c_r and growth rate $-\alpha_i$. Also shown in Fig. 16 are the slow acoustic and entropy/vorticity continuous spectra, which are a function of frequency, Reynolds number, and Mach number in the free stream. Further discussion of the continuous spectra and their calculation is available from Balakumar and Malik[61] and Tumin.[62–64] It should be noted that the continuous spectra calculations performed here are for a perfect gas and may not be entirely representative of this flow field. They are intended to be used as an approximation for visualizing synchronization. Mode F1$^+$ begins in the fast acoustic continuous spectrum (not pictured) and decreases in phase speed as streamwise distance s increases. Near c_r = 1, the second mode synchronizes with the continuous entropy/vorticity spectra (which are actually two overlapping branches). This interaction with the continuous modes causes a damping effect in mode F1$^+$. Fedorov and Tumin[59] noted that the boundary layer is particularly receptive to entropy/vorticity disturbances in this synchronism region. Further downstream, the mode becomes unstable. The point at which the mode first becomes unstable corresponds to the lower neutral branch on the stability curve. As s increases, the mode behaves differently for lower frequencies. At f = 800 kHz and above, the mode becomes stable before synchronizing with the slow acoustic spectrum ($c_r = 1 - 1/M_\infty$). The point at which the second mode becomes stable again corresponds to the upper branch of the neutral stability curve. The lower frequencies, however, synchronize while still unstable. This causes the cessation of mode F1$^+$ being discrete and causes the creation of the new discrete mode F1$^-$, shown by the dotted line in Fig. 16. Mode F1$^+$ remains unstable for longer along the body until it finally becomes stable and merges with the rest of the slow acoustic continuous spectrum. This delay in mode F1$^+$ becoming

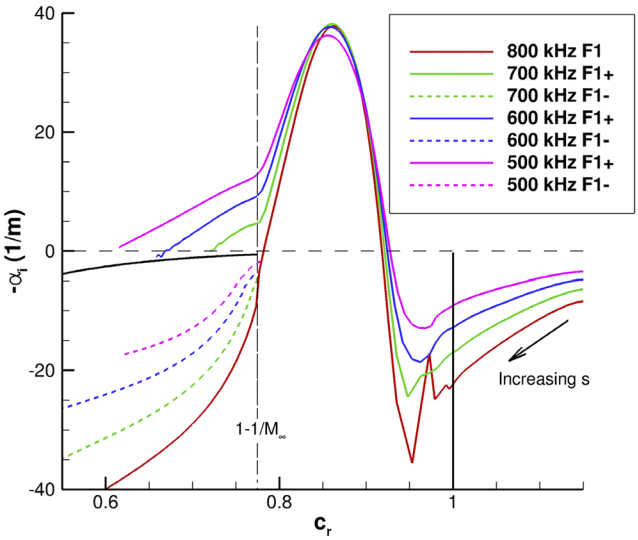

FIG. 16. Case 1 dispersion relation for second mode. Black lines correspond to the continuous spectra evaluated at M_∞ = 4.44, R = 1000, and $\Omega = RF$ = 0.4. Dashed lines indicate the new mode F1$^-$ created during synchronization with the slow acoustic spectrum.

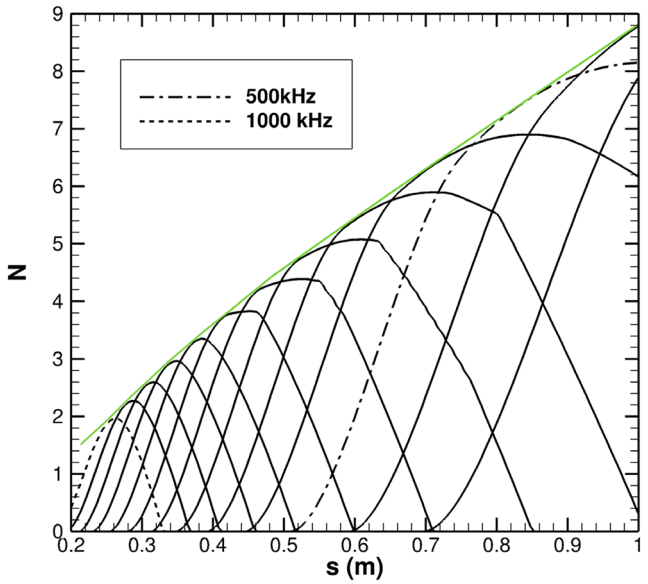

FIG. 17. Case 1 N-factor for unstable second mode frequencies. Frequencies are in increments of Δf = 50 kHz. The green line is an approximation of the edge of the N-factor curve. The frequency f = 450 kHz leads to the largest N-factor.

stable is visualized in the broadening of the region of instability, shown in the neutral stability map in Fig. 13. The synchronization of mode F1$^+$ with the slow acoustic spectrum is akin to the synchronization with the entropy/vorticity modes. Similarly, the boundary layer may be receptive to slow acoustic disturbances in the free stream near this region. However, as Bitter and Shepherd[26] have pointed out since the synchronism region is near the upper branch of the neutral curve, it is unlikely to cause significant amplifications to the second mode.

The mode F1$^+$ growth rate for each frequency was integrated along the surface numerically using the trapezoidal method to determine the N-factor curve for this particular case. The N-factor is presented as a function of streamwise distance s. Frequency increments of Δf = 50 kHz were used to obtain the N-factor results in Fig. 17. An N-factor of roughly 9 will be achieved by the end of the length of the 1 meter cone. Note the influence of the supersonic modes in changing the shape of the peaks of the N-factor for each frequency. For example, the high-frequency peaks (f = 1000 kHz, for example) are nearly symmetric. After the supersonic mode is encountered, the curve is elongated due to mode F1$^+$ being unstable. The elongated region of instability causes the N-factor curve to become asymmetric, and the peak of the curve occurs farther downstream. These supersonic modes seem to have only a small impact on the edge of the N-factor curve, however, as shown by the green line in Fig. 17. Because the supersonic mode occurs downstream of the maximum growth rate for each frequency, the N-factor for each frequency displays the elongated effect downstream of its peak N-factor, which does not affect the green N-factor envelope in Fig. 17. Therefore, the supersonic modes contribute very little to the maximum N-factor for this case. However, because this N-factor curve is only valid for the flow conditions in case 1, it is difficult to draw a definitive conclusion on the role of the supersonic modes in N-factor transition prediction methods. More cases with different flow conditions are necessary to evaluate the effect of the spontaneous radiation of sound on transition using the e^N method.

Finally, the temperature perturbation contour predicted by LST for a fixed wavenumber and frequency was created to demonstrate the role of the relative Mach number [Eq. (2)] in flows with the supersonic mode. The contour in Fig. 18 is obtained from

$$T'(s,y) = Real\left[\hat{T}e^{i(\alpha s+\beta z-\omega t)}\right], \tag{21}$$

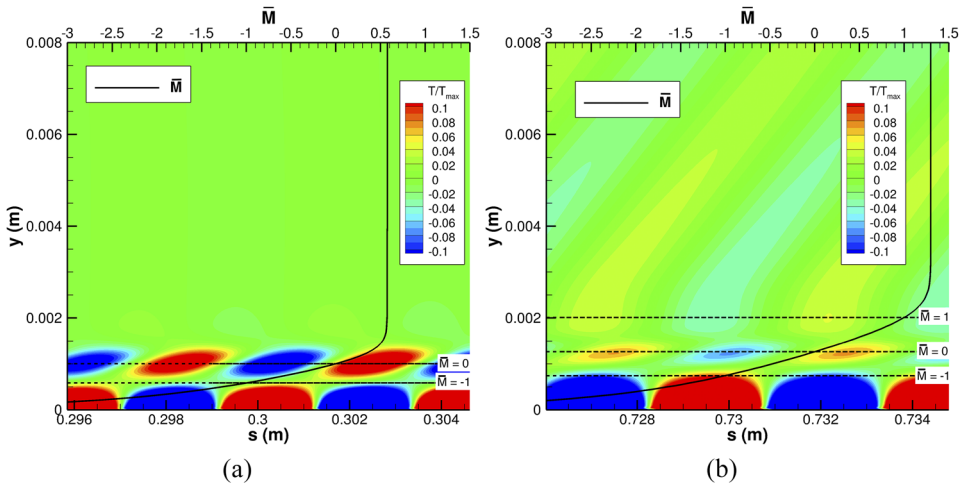

(a) (b)

FIG. 18. Case 1 LST temperature perturbation contours. (a) Subsonic mode: s = 0.302 m, f = 800 kHz and (b) supersonic mode: s = 0.733 m, f = 550 kHz.

where α is the complex wavenumber at the fixed streamwise location s_0 and frequency f_0 and $\hat{T}$ is the complex temperature eigenfunction at the fixed streamwise location s_0 and frequency f_0. The streamwise distance s is varied only slightly because in general, α and $\hat{T}$ are functions of s, making this technique invalid for regions far from s_0. The temperature perturbation contour at time $t = 0$ in Fig. 18 illustrates very clearly the distinct regions of the disturbance behavior summarized by the supersonic mode diagram in Fig. 2. For both the subsonic and supersonic modes, the first sonic line $\overline{M} = -1$ acts as a wave guide for the acoustic waves traveling downstream supersonically relative to the mean flow velocity. Centered about $\overline{M}$, the "rope-like" wave structures can be seen for both the supersonic and subsonic modes. However, outside of these "rope-like" wave structures is where the subsonic and supersonic modes differ fundamentally. For the subsonic mode [Fig. 18(a)], the relative Mach number does not exceed $\overline{M} = 0.6$. The relative Mach number for the supersonic mode [Fig. 18(b)], on the other hand, exceeds $\overline{M} = 1$ near the edge of the boundary layer (location at which $\overline{M}$ does not change greatly; similar to δ_{99}). The effect of this supersonic disturbance propagation is the "slanted" wave pattern in the free stream. Indeed, the angle this wave pattern makes is quite close with the predicted Mach angle $\mu \approx \arcsin(1/\overline{M}) = 50.3°$. The agreement is not exact due to the small imaginary component of α.

The results presented in this section indicate that the LST numerical methods used are capable of capturing the unique physics that occur when the second mode is unstable and traveling supersonically with respect to the free stream. Further analysis through unsteady DNS was performed to verify the phenomena predicted by the LST analysis.

B. Case 2 LST results

The growth rate and phase speed for the discrete modes of a $f = 700$ kHz disturbance are shown in Fig. 19. There are very notable differences in the stability characteristics between case 1 and case 2. In case 2, mode S appears to transitions into mode F1 upon synchronization near $s = 0.35$ m. Of course, the modes do not actually transition from one to another; rather it is an alternate behavior of mode S after synchronization with mode F1. This phenomenon is uncommon but has been encountered and analyzed by Ma and Zhong.[14] Furthermore, Fedorov and Tumin[5] have also encountered this seemingly strange stability characteristic, although it can be described by their model of discrete mode branching. This behavior still creates the possibility of a supersonic mode, however, due to the phase speed of the unstable mode S/F1 decreasing below $c_r < 1 - 1/M_\infty$. In the synchronization region of mode F1 with mode S, the weaker modes are difficult to identify with LST, resulting in the discontinuity in phase speed and growth rate. At this particular frequency of $f = 700$ kHz, the mode becomes stable prior to synchronization with the slow acoustic spectrum. Therefore, there is no unstable supersonic mode at this frequency. Interestingly, however, at lower frequencies below $f = 610$ kHz, the "transition" from mode S into mode F1 does not occur. Rather, mode F1 is the unstable mode just as in case 1, as shown in Fig. 20.

A neutral stability contour for case 2 [Fig. 21(a)] was created to determine if the supersonic mode was present at lower frequencies than $f = 700$ kHz. However, the upper branch of the neutral stability curve does not display a "kink" as it did in case 1, indicating that the supersonic mode is not present in case 2. For all frequencies, the unstable mode S/F1 becomes stable before obtaining a supersonic phase speed. Therefore, no unstable supersonic mode or sound radiation from the boundary layer is expected. This result agrees with the findings of Bitter and Shepherd[26] in that the supersonic mode is not encountered in the warmer wall temperature case. Nevertheless, it is still useful to compute the N-factor for case 2 to determine the effect the wall temperature has on transition. The N-factor curve for case 2 is shown in Fig. 21(b). The largest N-factor achieved by the end of the 1 meter long cone is approximately 5.5 and is due to the $f = 550$ kHz frequency. This is significantly lower than case 1, which had a

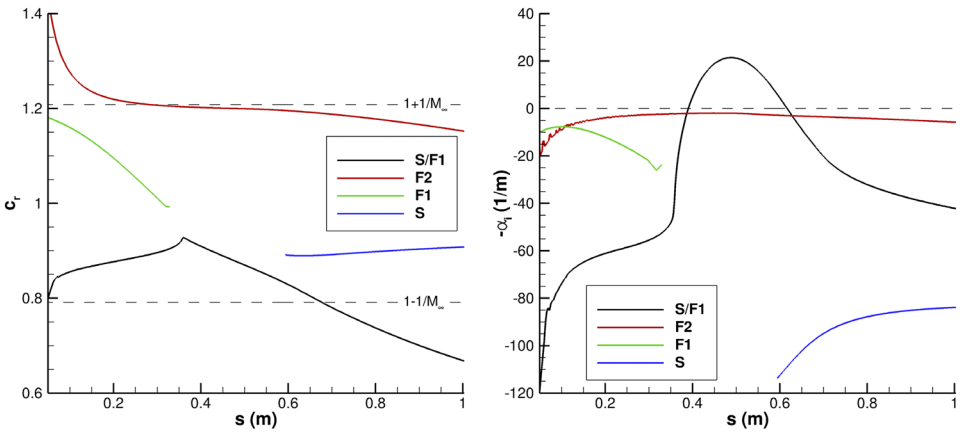

FIG. 19. Case 2 LST phase speed and growth rate for modes F1, F2, and S at $f = 700$ kHz. (a) Phase speed and (b) growth rate. $M_\infty = 4.44$ is the mean flow Mach number immediately downstream of the shock.

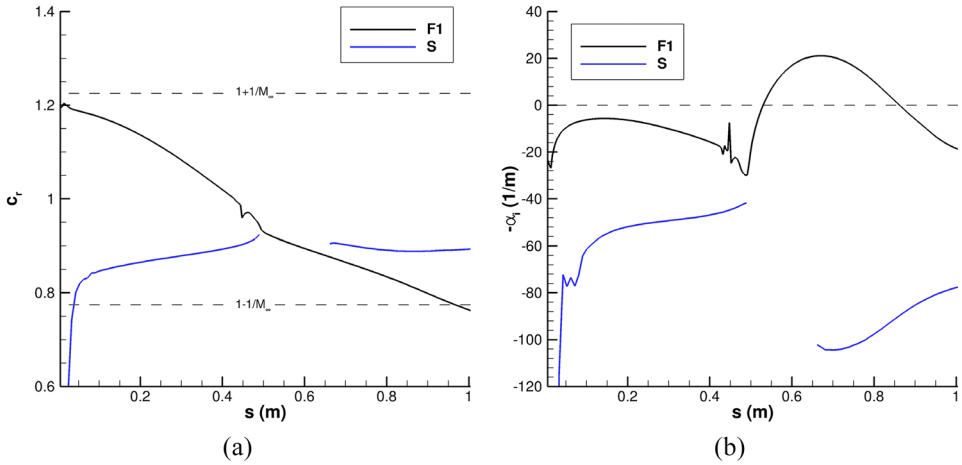

FIG. 20. Case 2 LST phase speed and growth rate for modes F1, F2, and S at f = 600 kHz. (a) Phase speed and (b) growth rate. M_∞ = 4.44 is the mean flow Mach number immediately downstream of the shock.

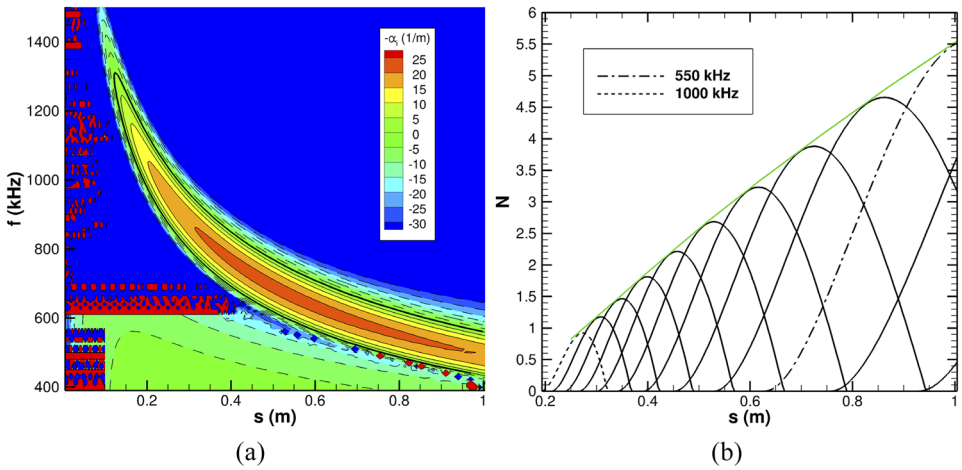

FIG. 21. Case 2 LST results. (a) Neutral stability map for second mode. Dashed lines indicate negative growth rates. The thick black line indicates the points of neutral stability. (b) N-factor for unstable second mode frequencies. Frequencies are in increments of Δf = 50 kHz. The green line is an approximation of the edge of the N-factor curve.

maximum N-factor of almost 9. This result is expected, however, as is well known that wall cooling destabilizes the second mode.

IX. DISCUSSION OF RESULTS AND CONCLUSION

New LST equations with $\bar{v} \neq 0$ and new LST shock boundary conditions were derived and verified with the application of more accurately studying the supersonic mode in an axisymmetric Mach 5 flow over a blunt 1 mm nose radius isothermal cold-wall cone. Two cases were considered: case 1 with a highly cooled wall (T_w/T_∞ = 0.2) and case 2 with a more moderately cooled wall (T_w/T_∞ = 0.667). Assuming $\bar{v}$ = 0 underpredicts the growth rate of a supersonic mode but has very little impact on subsonic modes. Therefore, it is important to include these nonparallel effects when studying the supersonic mode. The LST shock boundary conditions do not have a significant impact when the mean flow extends well beyond the boundary layer edge to allow the oscillatory perturbation to decay. The steady flow fields for both case 1 and case 2 showed strong thermochemical nonequilibrium effects in the nose region; however, the chemical nonequilibrium effects became less significant farther downstream. Thermochemical nonequilibrium LST analysis was performed on the mean flow to identify unstable modes and prescribe conditions for the unsteady DNS conditions used in Paper II.[65]

The supersonic mode has been shown to exist on an axisymmetric cone through LST analysis for case 1 (T_w/T_∞ = 0.2); however, no supersonic mode was found for case 2 (T_w/T_∞ = 0.667). These findings on an axisymmetric blunt cone with thermochemical nonequilibrium effects reinforce the results obtained for the flat plate geometry by Bitter and Shepherd[26] and Chuvakhov and Fedorov[27,28] that the cold wall is destabilizing to the supersonic mode. The formation of the unstable supersonic modes is only predicted by LST for an individual frequency as a peculiarity of the synchronization of the unstable discrete boundary layer mode F1 and the

continuous slow acoustic spectrum. Upon synchronization with the slow acoustic spectrum, an unstable mode F1 bifurcates into two simultaneously coexisting modes: the unstable mode F1$^+$ and the stable mode F1$^-$. Mode F1$^+$ gradually joins the slow acoustic spectrum and becomes stable, whereas mode F1$^-$ becomes increasingly stable as the streamwise distance increases.

LST analysis has also shown that the relative Mach number plays a critical role in the structure of the boundary layer disturbances. Specifically, below the first sonic line $\overline{M}(y_{s1}) = -1$ the disturbance travels downstream supersonically with respect to the mean flow. Between the two sonic lines $\overline{M}(y_{s1}) = -1$ and $\overline{M}(y_{s2}) = 1$, the disturbance travels subsonically with respect to the mean flow, resulting in "rope-like" structures centered about the critical layer $\overline{M}(y_c) = 0$. For supersonic modes, there exists a second sonic line at $\overline{M}(y_{s2}) = 1$, outside of which the disturbance travels upstream supersonically with respect to the mean flow, resulting in "slanted" wave patterns at an angle $\mu \approx \arcsin(1/\overline{M})$.

Overall, the radiation of sound by the supersonic mode has been shown to coincide with the synchronization of an unstable mode F1 with the slow acoustic spectrum. Because it is difficult to resolve the behavior of the boundary layer modes in the vicinity of this synchronization with LST, further analysis using DNS is required to fully understand the mechanism of the supersonic mode. This task is performed in Paper II,[65] which indicates the presence of the supersonic mode in both case 1 ($T_w/T_\infty = 0.2$) and case 2 ($T_w/T_\infty = 0.667$), in contrast to LST predictions. The mechanism of the supersonic mode is attributed to the interaction of the unstable subsonic mode S, stable supersonic mode F1, and the slow acoustic spectrum. LST assumes that each mode acts independently, however, and consequently the supersonic mode is not resolved with LST in all cases. Therefore, performing such a joint study of LST and DNS is necessary to reliably assess the impact of the supersonic mode on transition to turbulence.

ACKNOWLEDGMENTS

This research was supported by the U.S. Air Force Office of Scientific Research (AFOSR) through the National Defense Science & Engineering Graduate (NDSEG) Fellowship Program. This research was also partially supported by the AFOSR, USAF, under AFOSR Grant No. FA9550-15-1-0268, monitored by Dr. Ivett Leyva, and by the Office of Naval Research (ONR) under Grant No. N00014-17-1-2343, monitored by Dr. Eric Marineau currently and by Dr. Knox Millsaps previously. Primary computational resources were provided by the AFOSR with additional computational resources provided by Extreme Science and Engineering Discovery Environment (XSEDE) through Texas Advanced Computing Center (TACC) and San Diego Supercomputer Center (SDSC) under Grant No. TG-ASC090076, supported in part by the National Science Foundation. Thanks to Michael Miselis for his calculation of the continuous spectra. The views and conclusions contained herein are those of the authors and should not be interpreted as necessarily representing the official policies or endorsements, either expressed or implied, of the U.S. Air Force Office of Scientific Research, the Office of Naval Research, or the U.S. Government.

APPENDIX A: LST MATRIX ELEMENTS

The nonzero elements of each complex matrix for the nonequilibrium LST perturbation equations are given below, where $\vec{\phi} = [\hat{\rho}_1, \hat{\rho}_2, \ldots, \hat{\rho}_{ns}, \hat{u}, \hat{v}, \hat{w}, \hat{T}, \hat{T}_V]^T$ and δ_{ij} is the Kronecker delta. The subscripts $i, j = 1, 2, \ldots, ns$, where ns is the number of species in the model. The overbars indicating the steady mean flow components have been dropped for simplicity. Elemental lengths are defined as $h_1 dx$, dy, and $h_3 dz$, where

$$h_1 = 1 + \kappa y, \tag{A1}$$

$$h_3 = r_b + y\cos(\theta) \tag{A2}$$

and where κ is the streamwise curvature, r_b is the local radius of the body, and θ is the local half angle of the body. The coordinate system for a flat plate is recovered by setting h_1 and h_3 to unity. For a straight cone, only h_3 is required and h_1 is set to unity. The grid transformation effects are incorporated by

$$\alpha_0 = \frac{\alpha}{h_1},$$

$$\beta_0 = \frac{\beta}{h_3},$$

$$m_{11} = \frac{1}{h_1}\frac{\partial h_1}{\partial y},$$

$$m_{13} = \frac{1}{h_1 h_3}\frac{\partial h_3}{\partial x},$$

$$m_{33} = \frac{1}{h_3}\frac{\partial h_3}{\partial y}.$$

The LST perturbation equation is repeated here for clarity

$$\left(\mathbf{A}\frac{d^2}{dy^2} + \mathbf{B}\frac{d}{dy} + \mathbf{C}\right)\vec{\phi} = \vec{0},$$

where the nonzero components of matrices **A**, **B**, **C** are

$$A_{i,j} = D_i(c_i - \delta_{ij}),$$

$$A_{ns+1,ns+1} = 1,$$

$$A_{ns+2,ns+2} = 1,$$

$$A_{ns+3,ns+3} = 1,$$

$$A_{ns+4,j} = \sum_{s=1}^{ns} h_s D_s c_s - h_j D_j,$$

$$A_{ns+4,ns+4} = -k,$$

$$A_{ns+4,ns+5} = -k_V,$$

$$A_{ns+5,j} = \sum_{s=1}^{ns} e_{vs} D_s c_s - e_{vj} D_j,$$

$$A_{ns+5,ns+5} = -k_V,$$

$$B_{i,j} = \delta_{ij}\left[v - \rho\frac{d}{dy}\left(\frac{D_i}{\rho}\right) - (m_{11}+m_{33})D_i\right] + \rho\frac{d}{dy}\left(\frac{D_i c_i}{\rho}\right) + \left(c_i\frac{d\rho}{dy} - \frac{d\rho_i}{dy}\right)\frac{\partial D_i}{\partial \rho_j} + (m_{11}+m_{33})D_i c_i,$$

$$B_{i,ns+2} = \rho_i,$$

$$B_{i,ns+4} = \left(c_i\frac{d\rho}{dy} - \frac{d\rho_i}{dy}\right)\frac{\partial D_i}{\partial T},$$

$$B_{ns+1,j} = \frac{1}{\mu}\frac{d\mu}{d\rho_j}\left(\frac{du}{dy} - m_{11}u\right),$$

$$B_{ns+1,ns+1} = \frac{1}{\mu}\frac{d\mu}{dy} + m_{11} + m_{33} - \frac{1}{\mu}\rho v,$$

$$B_{ns+1,ns+2} = \frac{1}{3}i\alpha_0,$$

$$B_{ns+1,ns+4} = \frac{1}{\mu}\frac{\partial\mu}{\partial T}\left(\frac{du}{dy} - m_{11}u\right),$$

$$B_{ns+2,j} = -\frac{3}{4}\frac{1}{\mu}\frac{\mathcal{R}}{M_j} - \frac{1}{2}\frac{1}{\mu}\frac{\partial\mu}{\partial\rho_j}[m_{13}u + (m_{11}+m_{33})v] + \frac{1}{\mu}\frac{\partial\mu}{\partial\rho_j}\frac{dv}{dy},$$

$$B_{ns+2,ns+1} = \frac{1}{4}(m_{13} + i\alpha_0),$$

$$B_{ns+2,ns+2} = \frac{1}{\mu}\frac{d\mu}{dy} + m_{11} + m_{33} - \frac{3}{4}\frac{1}{\mu}\rho v,$$

$$B_{ns+2,ns+3} = \frac{1}{4}i\beta_0,$$

$$B_{ns+2,ns+4} = -\frac{3}{4}\frac{1}{\mu}\frac{p}{T} - \frac{1}{2}\frac{1}{\mu}\frac{\partial\mu}{\partial T}[m_{13}u + (m_{11}+m_{33})v] + \frac{1}{\mu}\frac{\partial\mu}{\partial T}\frac{dv}{dy},$$

$$B_{ns+3,ns+2} = \frac{1}{3}i\beta_0,$$

$$B_{ns+3,ns+3} = \frac{1}{\mu}\frac{d\mu}{dy} + m_{11} + m_{33} - \frac{3}{4}\frac{1}{\mu}\rho v,$$

$$B_{ns+4,j} = v\left(Tc_{v,j} + e_{vj} + h_j^o\right) - \frac{dT}{dy}\frac{\partial k}{\partial\rho_j} - \frac{dT_V}{dy}\frac{\partial k_V}{\partial\rho_j} + \sum_{s=1}^{ns} h_s\left(c_s\frac{d\rho}{dy} - \frac{d\rho_s}{dy}\right)\frac{\partial D_s}{\partial\rho_j} + \rho\frac{d}{dy}\left[\frac{1}{\rho}\left(\sum_{s=1}^{ns} h_s D_s c_s - h_j D_j\right)\right] + (m_{11}+m_{33})\left(\sum_{s=1}^{ns} h_s D_s c_s - h_j D_j\right),$$

$$B_{ns+4,ns+1} = 2\mu\left(m_{11}u - \frac{du}{dy}\right),$$

$$B_{ns+4,ns+2} = \frac{4}{3}\mu\left(m_{13}u + (m_{11}+m_{33})v - 2\frac{dv}{dy}\right) + p + T\sum_{s=1}^{ns}\rho_s c_{v,s} + \sum_{s=1}^{ns}\rho_s e_{vs} + \sum_{s=1}^{ns}\rho_s h_s^o,$$

$$B_{ns+4,ns+4} = \rho c_v v - \frac{dk}{dy} - \frac{dT}{dy}\frac{\partial k}{\partial T} - \frac{dT_V}{dy}\frac{\partial k_V}{\partial T} - (m_{11}+m_{33})k + \sum_{s=1}^{ns} h_s\left(c_s\frac{d\rho}{dy} - \frac{d\rho_s}{dy}\right)\frac{\partial D_s}{\partial T} + \sum_{s=1}^{ns} D_s\left(c_s\frac{d\rho}{dy} - \frac{d\rho_s}{dy}\right)\left(c_{v,s} + \frac{\mathcal{R}}{M_s}\right),$$

$$B_{ns+4,ns+5} = v\sum_{s=1}^{ns}\rho_s\frac{\partial e_{vs}}{\partial T_V} - \frac{dk_V}{dy} - \frac{dT_V}{dy}\frac{\partial k_V}{\partial T_V} - (m_{11}+m_{33})k_V + \sum_{s=1}^{ns} D_s\left(c_s\frac{d\rho}{dy} - \frac{d\rho_s}{dy}\right)\frac{\partial e_{vs}}{\partial T_V},$$

$$B_{ns+5,j} = -\frac{dT_V}{dy}\frac{\partial k_V}{\partial\rho_j} + \rho\frac{d}{dy}\left[\frac{1}{\rho}\left(\sum_{s=1}^{ns} e_{vs} D_s c_s - e_{vj} D_j\right)\right] + \sum_{s=1}^{ns} e_{vs}\left(c_s\frac{d\rho}{dy} - \frac{d\rho_s}{dy}\right)\frac{\partial D_s}{\partial\rho_j} + (m_{11}+m_{33})\left(\sum_{s=1}^{ns} e_{vs} D_s c_s - e_{vj} D_j\right) + v e_{vj},$$

$$B_{ns+5,ns+2} = \sum_{s=1}^{ns} \rho_s e_{vs},$$

$$B_{ns+5,ns+4} = -\frac{dT_V}{dy}\frac{\partial k_V}{\partial T} + \sum_{s=1}^{ns} e_{vs}\left(c_s\frac{d\rho}{dy} - \frac{d\rho_s}{dy}\right)\frac{\partial D_s}{\partial T},$$

$$B_{ns+5,ns+5} = v\sum_{s=1}^{ns}\rho_s\frac{\partial e_{vs}}{\partial T_V} - \frac{dk_V}{dy} - \frac{dT_V}{dy}\frac{\partial k_V}{\partial T_V} + \sum_{s=1}^{ns} D_s\left(c_s\frac{d\rho}{dy} - \frac{d\rho_s}{dy}\right)\frac{\partial e_{vs}}{\partial T_V} - (m_{11}+m_{33})k_V,$$

$$C_{i,j} = \delta_{ij}\left[i(\alpha_0(u - m_{13}D_i) - \omega) + D_i(\alpha_0^2+\beta_0^2)\right] + D_i c_i\left[i\alpha_0 m_{13} - (\alpha_0^2+\beta_0^2)\right] + \delta_{ij}\left[m_{13}u + (m_{11}+m_{33})v + \frac{dv}{dy} + \frac{d}{dy}\left(\frac{D_i}{\rho}\frac{d\rho}{dy}\right) + (m_{11}+m_{33})\frac{D_i}{\rho}\frac{d\rho}{dy}\right] - \frac{\partial\omega_i}{\partial\rho_j} + (m_{11}+m_{33})\left[\left(c_i\frac{d\rho}{dy} - \frac{d\rho_i}{dy}\right)\frac{\partial D_i}{\partial\rho_j} - \frac{D_i c_i}{\rho}\frac{d\rho}{dy}\right] - \frac{d}{dy}\left(\frac{D_i c_i}{\rho}\frac{d\rho}{dy}\right) + \frac{d}{dy}\left[\left(c_i\frac{d\rho}{dy} - \frac{d\rho_i}{dy}\right)\frac{\partial D_i}{\partial\rho_j}\right],$$

$$C_{i,ns+1} = \rho_i(i\alpha_0 + m_{13}),$$

$$C_{i,ns+2} = \frac{d\rho_i}{dy} + (m_{11}+m_{33})\rho_i,$$

$$C_{i,ns+3} = i\beta_0\rho_i,$$

$$C_{i,ns+4} = \frac{d}{dy}\left[\left(c_i\frac{d\rho}{dy} - \frac{d\rho_i}{dy}\right)\frac{\partial D_i}{\partial T}\right] + (m_{11}+m_{33})\left(c_i\frac{d\rho}{dy} - \frac{d\rho_i}{dy}\right)\frac{\partial D_i}{\partial T} - \frac{\partial\omega_i}{\partial T},$$

$$C_{i,ns+5} = -\frac{\partial\omega_i}{\partial T_V},$$

$$C_{ns+1,j} = i\alpha_0\left[\frac{4}{3}\frac{1}{\mu}m_{11}v\frac{\partial\mu}{\partial\rho_j} - \frac{2}{3}\frac{1}{\mu}\left(m_{13}u + m_{33}v + \frac{dv}{dy}\right)\frac{\partial\mu}{\partial\rho_j} - \frac{1}{\mu}\frac{\mathcal{R}}{M_j}T\right] + \frac{1}{\mu}\frac{d}{dy}\left(\frac{du}{dy}\frac{\partial\mu}{\partial\rho_j}\right) + \frac{1}{\mu}\left[(m_{11}+m_{33})\frac{du}{dy} + vm_{13}\left(2m_{11} - \frac{4}{3}m_{33}\right) - u\left(m_{11}^2 + m_{11}m_{33} + \frac{4}{3}m_{13}^2\right)\right] - \frac{1}{\mu}v\frac{du}{dy} - \frac{1}{\mu}m_{11}u\frac{d}{dy}\left(\frac{\partial\mu}{\partial\rho_j}\right),$$

$$C_{ns+1,ns+1} = i\left[\alpha_0\left(\frac{4}{3}m_{13} - \frac{1}{\mu}\rho u\right) - \frac{1}{\mu}\omega\rho\right] - m_{11}\left(\frac{1}{\mu}\rho v + \frac{1}{\mu}\frac{d\mu}{dy} + m_{11} + m_{33}\right) - \frac{4}{3}m_{13}^2 - \frac{4}{3}\alpha_0^2 - \beta_0^2,$$

$$C_{ns+1,ns+2} = i\alpha_0\left(\frac{7}{3}m_{11} + \frac{1}{3}m_{33} + \frac{1}{\mu}\frac{d\mu}{dy}\right) - \rho\frac{1}{\mu}\frac{du}{dy} - m_{11}\frac{1}{\mu}\rho u + m_{13}\left(2m_{11} - \frac{4}{3}m_{33}\right),$$

$$C_{ns+1,ns+3} = -\beta_0\left(\frac{7}{3}im_{13} + \frac{1}{3}\alpha_0\right),$$

$$C_{ns+1,ns+4} = i\alpha_0\left[\frac{\partial\mu}{\partial T}\left(\frac{4}{3}m_{11}v - \frac{2}{3}m_{33}v - \frac{2}{3}\frac{dv}{dy} - \frac{2}{3}m_{13}u\right) - \frac{p}{T}\right] - \frac{1}{\mu}m_{11}u\frac{d}{dy}\left(\frac{\partial\mu}{\partial T}\right) + \frac{1}{\mu}\frac{\partial\mu}{\partial T}\left[m_{13}v\left(2m_{11} - \frac{4}{3}m_{33}\right) - u\left(m_{11}^2 + m_{11}m33 + \frac{4}{3}m_{13}^2\right) + (m_{11}+m_{33})\frac{du}{dy}\right] + \frac{1}{\mu}\frac{d}{dy}\left(\frac{du}{dy}\frac{\partial\mu}{\partial T}\right),$$

$$C_{ns+2,j} = i\alpha_0\frac{3}{4}\frac{1}{\mu}\frac{\partial\mu}{\partial\rho_j}\left(\frac{du}{dy} - m_{11}u\right) - \frac{3}{4}\frac{1}{\mu}v\frac{dv}{dy} - \frac{3}{4}\frac{1}{\mu}\frac{\mathcal{R}}{M_j}\frac{dT}{dy} + \frac{1}{\mu}\frac{d}{dy}\left(\frac{dv}{dy}\frac{\partial\mu}{\partial\rho_j}\right) + \frac{3}{4}\frac{1}{\mu}m_{11}u^2 + \frac{1}{\mu}\frac{\partial\mu}{\partial\rho_j}\left[\frac{1}{4}m_{13}\frac{du}{dy} - m_{13}u\left(\frac{1}{4}m_{11} + m_{33}\right) - v\left(m_{11}^2 + m_{33}^2\right) + (m_{11}+m_{33})\frac{dv}{dy}\right] - \frac{1}{2}\frac{1}{\mu}[m_{13}u + (m_{11}+m_{33})v]\frac{d}{dy}\left(\frac{\partial\mu}{\partial\rho_j}\right),$$

$$C_{ns+2,ns+1} = -i\alpha_0\left(\frac{1}{2}\frac{1}{\mu}\frac{d\mu}{dy} + \frac{7}{4}m_{11}\right) + \frac{3}{2}\frac{1}{\mu}m_{11}\rho u - m_{13}\left(\frac{1}{4}m_{11} - m_{33} - \frac{1}{2}\frac{1}{\mu}\frac{d\mu}{dy}\right),$$

$$C_{ns+2,ns+2} = \frac{3}{4}i\left[\omega\rho - \alpha_0\left(\frac{1}{\mu}\rho u - m_{13}\right)\right] - \frac{3}{4}\left(\alpha_0^2+\beta_0^2\right) - \frac{3}{4}\frac{1}{\mu}\rho\frac{dv}{dy} - \frac{1}{2}(m_{11}+m_{33})\frac{1}{\mu}\frac{d\mu}{dy} - \left(m_{11}^2 + m_{33}^2\right),$$

$$C_{ns+2,ns+3} = -i\beta_0\left(\frac{1}{2}\frac{1}{\mu}\frac{d\mu}{dy} + \frac{7}{4}m_{33}\right),$$

$$C_{ns+2,ns+4} = \frac{3}{4}i\alpha_0\frac{1}{\mu}\left(\frac{du}{dy} - m_{11}u\right)\frac{\partial\mu}{\partial T} - \frac{1}{2}\frac{1}{\mu}[m_{13}u + (m_{11}+m_{33})v]\frac{d}{dy}\left(\frac{\partial\mu}{\partial T}\right) - \frac{3}{4}\frac{1}{\mu}\frac{d}{dy}\left(\frac{p}{T}\right) + \frac{1}{\mu}\frac{\partial\mu}{\partial T}\left[-m_{13}u\left(\frac{1}{4}m_{11}+m_{33}\right) - v\left(m_{11}^2+m_{33}^2\right) + \frac{1}{4}m_{13}\frac{du}{dy} + (m_{11}+m_{33})\frac{dv}{dy}\right] + \frac{1}{\mu}\frac{d}{dy}\left(\frac{dv}{dy}\frac{\partial\mu}{\partial T}\right),$$

$$C_{ns+3,j} = -i\beta_0\frac{1}{\mu}\left[\frac{\mathcal{R}}{M_j}T - \frac{4}{3}\frac{\partial\mu}{\partial\rho_j}(m_{13}u + m_{33}v) + \frac{2}{3}\frac{\partial\mu}{\partial\rho_j}\left(m_{11}v + \frac{dv}{dy}\right)\right],$$

$$C_{ns+3,ns+1} = i\beta_0\left(\frac{7}{3}m_{13} - \frac{1}{3}\alpha_0\right),$$

$$C_{ns+3,ns+2} = i\beta_0\left(\frac{1}{\mu}\frac{d\mu}{dy} + \frac{1}{3}m_{11} + \frac{7}{3}m_{33}\right),$$

$$C_{ns+3,ns+3} = i\left[\frac{1}{\mu}\omega\rho + \alpha_0\left(m_{13} - \frac{1}{\mu}\rho u\right)\right] - m_{13}\frac{1}{\mu}\rho u - m_{33}\frac{1}{\mu}\rho v - m_{13}^2 - m_{33}^2 - m_{11}m_{33} - m_{33}\frac{1}{\mu}\frac{d\mu}{dy} - \alpha_0^2 - \frac{4}{3}\beta_0^2,$$

$$C_{ns+3,ns+4} = -i\beta_0\frac{1}{\mu}\left[\frac{p}{T} - \frac{4}{3}\frac{\partial\mu}{\partial T}(m_{13}u + m_{33}v) + \frac{2}{3}\frac{\partial\mu}{\partial T}\left(m_{11}v + \frac{dv}{dy}\right)\right],$$

$$C_{ns+4,j} = i\left[(\alpha_0 u - \omega)\left(Tc_{v,j} + e_{vj} + h_j^o\right) + \alpha_0 m_{13}\left(\sum_{s=1}^{ns} D_s c_s h_s - h_j D_j\right)\right] - \frac{d}{dy}\left(\frac{dT}{dy}\frac{\partial k}{\partial\rho_j}\right) - \frac{d}{dy}\left(\frac{dT_V}{dy}\frac{\partial k_V}{\partial\rho_j}\right) + [m_{13}u + (m_{11}+m_{33})v]\left(Tc_{v,j} + e_{vj} + h_j^o + \frac{\mathcal{R}}{M_j}T\right) + \frac{d}{dy}\left[v\left(Tc_{v,j} + e_{vj} + h_j^o + \frac{\mathcal{R}}{M_j}T\right)\right] - (m_{11}+m_{33})\left(\frac{dT}{dy}\frac{\partial k}{\partial\rho_j} + \frac{dT_V}{dy}\frac{\partial k_V}{\partial\rho_j}\right) + \frac{\partial\mu}{\partial\rho_j}\left[-\frac{4}{3}v^2\left(m_{11}^2 + m_{33}^2 + m_{11}m_{33}\right) - \frac{4}{3}\left(\frac{dv}{dy}\right)^2 - u^2\left(\frac{4}{3}m_{13}^2 + m_{11}^2\right) - \left(\frac{du}{dy}\right)^2\right] + \frac{\partial\mu}{\partial\rho_j}\left[\frac{4}{3}uvm_{13}(m_{11} - 2m_{33}) + \frac{4}{3}v\frac{dv}{dy}(m_{11}+m_{33}) + \frac{4}{3}u\frac{dv}{dy}m_{13} + 2m_{11}u\frac{du}{dy}\right] + \frac{d}{dy}\left(\sum_{s=1}^{ns} h_s\left(c_s\frac{d\rho}{dy} - \frac{d\rho_s}{dy}\right)\frac{\partial D_s}{\partial\rho_j}\right) + \frac{d}{dy}\left(\frac{h_j D_j}{\rho}\frac{d\rho}{dy}\right) + h_j D_j(\alpha_0^2 + \beta_0^2) + (m_{11}+m_{33})\left[\sum_{s=1}^{ns} h_s\left(c_s\frac{d\rho}{dy} - \frac{d\rho_s}{dy}\right)\frac{\partial D_s}{\partial\rho_j}\right] - \frac{d}{dy}\left(\sum_{s=1}^{ns}\frac{h_s D_s c_s}{\rho}\frac{d\rho}{dy}\right) - \sum_{s=1}^{ns} h_s D_s c_s(\alpha_0^2 + \beta_0^2) + (m_{11}+m_{33})\frac{1}{\rho}\frac{d\rho}{dy}\left(h_j D_j - \sum_{s=1}^{ns} h_s D_s c_s\right),$$

$$C_{ns+4,ns+1} = \frac{4}{3}i\alpha_0\mu\left(m_{13}u + m_{33}v + \frac{dv}{dy} - 2m_{11}v\right) + i\alpha_0\left(p + T\rho c_v + E_V + \sum_{s=1}^{ns}\rho_s h_s^o\right) + 2\mu\left[m_{13}v\left(\frac{2}{3}m_{11} - \frac{4}{3}m_{33}\right) - u\left(\frac{4}{3}m_{13}^2 + m_{11}^2\right) + \frac{2}{3}m_{13}\frac{dv}{dy} + m_{11}\frac{du}{dy}\right] + m_{13}\left(p + T\rho c_v + E_V + \sum_{s=1}^{ns}\rho_s h_s^o\right),$$

$$C_{ns+4,ns+2} = -2\mu i\alpha_0\left(\frac{du}{dy} - m_{11}u\right) + \frac{d}{dy}\left(\sum_{s=1}^{ns}\rho_s c_{v,s}T\right) + \sum_{s=1}^{ns}\frac{d\rho_s}{dy}h_s^0 + \frac{4}{3}\mu\left[m_{13}u(m_{11} - 2m_{33}) + 2v\left(m_{11}m_{33} - m_{11}^2 - m_{33}^2\right) + (m_{11}+m_{33})\frac{dv}{dy}\right] + (m_{11}+m_{33})\left(p + T\rho c_v + E_V + \sum_{s=1}^{ns}\rho_s h_s^o\right),$$

$$C_{ns+4,ns+3} = i\beta_0\left[p + T\rho c_v + E_V + \sum_{s=1}^{ns}\rho_s h_s^o + \frac{4}{3}\mu\left(-2m_{13}u + v(m_{11} - 2m_{33}) + \frac{dv}{dy}\right)\right],$$

$$\begin{aligned}C_{ns+4,ns+4} = {} & i[\alpha_0(\rho u c_v - m_{13}k) - \omega\rho c_v] + (\alpha_0^2 + \beta_0^2)k + \rho c_v\frac{dc_v}{dy} - \frac{d}{dy}\left(\frac{dT}{dy}\frac{\partial k}{\partial T}\right) - \frac{d}{dy}\left(\frac{dT_V}{dy}\frac{\partial k_V}{\partial T}\right)\\ & + \left(\rho c_v + \frac{p}{T}\right)\left[m_{13}u + (m_{11} + m_{33})v + \frac{dv}{dy}\right] + \frac{\partial\mu}{\partial T}\left[\frac{4}{3}v^2(m_{11}m_{33} - m_{11}^2 - m_{33}^2)\right.\\ & \left. + \frac{4}{3}uvm_{13}(m_{11} - 2m_{33}) + \frac{4}{3}v\frac{dv}{dy}(m_{11} + m_{33})\right] + \frac{\partial\mu}{\partial T}\left[-\frac{4}{3}\left(\frac{dv}{dy}\right)^2 + \frac{4}{3}u\frac{dv}{dy}m_{13} - u^2\left(\frac{4}{3}m_{13}^2 + m_{11}^2\right)\right.\\ & \left. + 2m_{11}u\frac{du}{dy} - \left(\frac{du}{dy}\right)^2\right] + \frac{d}{dy}\left[\sum_{s=1}^{ns}h_s\left(c_s\frac{d\rho}{dy} - \frac{d\rho_s}{dy}\right)\frac{\partial D_s}{\partial T}\right] + \sum_{s=1}^{ns}\left(c_{v,s} + \frac{\mathcal{R}}{M_s}\right)\frac{d}{dy}\left[D_s\left(c_s\frac{d\rho}{dy} - \frac{d\rho_s}{dy}\right)\right]\\ & + (m_{11} + m_{33})\left[\sum_{s=1}^{ns}h_s\left(c_s\frac{d\rho}{dy} - \frac{d\rho_s}{dy}\right)\frac{\partial D_s}{\partial T} + \sum_{s=1}^{ns}\left(c_{v,s} + \frac{\mathcal{R}}{M_s}\right)D_s\left(c_s\frac{d\rho}{dy} - \frac{d\rho_s}{dy}\right)\right]\\ & - (m_{11} + m_{33})\left[\frac{dT}{dy}\frac{\partial k}{\partial T} + \frac{dT_V}{dy}\frac{\partial k_V}{\partial T}\right],\end{aligned}$$

$$\begin{aligned}C_{ns+4,ns+5} = {} & i\left[\alpha_0\left(u\sum_{s=1}^{ns}\rho_s\frac{\partial e_{vs}}{\partial T_V} - m_{13}k_V\right) - \omega\sum_{s=1}^{ns}\rho_s\frac{\partial e_{vs}}{\partial T_V}\right] + v\frac{d}{dy}\left(\sum_{s=1}^{ns}\rho_s\frac{\partial e_{vs}}{\partial T_V}\right)\\ & + \left(m_{13}u + (m_{11} + m_{33})v + \frac{dv}{dy}\right)\sum_{s=1}^{ns}\rho_s\frac{\partial e_{vs}}{\partial T_V} + (\alpha_0^2 + \beta_0^2)k_V - \frac{d}{dy}\left(\frac{dT_V}{dy}\frac{\partial k_V}{\partial T_V}\right)\\ & - (m_{11} + m_{33})\frac{dT_V}{dy}\frac{\partial k_V}{\partial T_V} + (m_{11} + m_{33})\left[\sum_{s=1}^{ns}D_s\left(c_s\frac{d\rho}{dy} - \frac{d\rho_s}{dy}\right)\frac{\partial e_{vs}}{\partial T_V}\right] + \frac{d}{dy}\left[\sum_{s=1}^{ns}D_s\left(c_s\frac{d\rho}{dy} - \frac{d\rho_s}{dy}\right)\frac{\partial e_{vs}}{\partial T_V}\right],\end{aligned}$$

$$\begin{aligned}C_{ns+5,j} = {} & i\left[\alpha_0\left(ue_{vj} + m_{13}\left(\sum_{s=1}^{ns}e_{vs}D_sc_s - e_{vj}D_j\right)\right) - \omega e_{vj}\right] - \sum_{s=1}^{ns}e_{vs}\frac{\partial\omega_s}{\partial\rho_j} - \frac{\partial Q_{T-V}}{\partial\rho_j} - \frac{d}{dy}\left(\frac{dT_V}{dy}\frac{\partial k_V}{\partial\rho_j}\right)\\ & + \left(\alpha_0^2 + \beta_0^2\right)\left[e_{vj}D_j - \sum_{s=1}^{ns}e_{vs}D_sc_s\right] + e_{vj}\left[m_{13}u + (m_{11} + m_{33})v + \frac{dv}{dy}\right] - \frac{d}{dy}\left(\frac{dT_V}{dy}\frac{\partial k_V}{\partial\rho_j}\right)\\ & - (m_{11} + m_{33})\frac{dT_V}{dy}\frac{\partial k_V}{\partial\rho_j} + \frac{d}{dy}\left(e_{vj}D_j\frac{1}{\rho}\frac{d\rho}{dy}\right) - \frac{d}{dy}\left(\sum_{s=1}^{ns}\frac{e_{vs}D_sc_s}{\rho}\frac{d\rho}{dy}\right) + \frac{d}{dy}\left(\sum_{s=1}^{ns}e_{vs}\left(c_s\frac{d\rho}{dy} - \frac{d\rho_s}{dy}\right)\frac{\partial D_s}{\partial\rho_j}\right)\\ & + (m_{11} + m_{33})\left[e_{vj}D_j\frac{1}{\rho}\frac{d\rho}{dy} - \sum_{s=1}^{ns}\frac{e_{vs}D_sc_s}{\rho}\frac{d\rho}{dy}\sum_{s=1}^{ns}e_{vs}\left(c_s\frac{d\rho}{dy} - \frac{d\rho_s}{dy}\right)\frac{\partial D_s}{\partial\rho_j}\right],\end{aligned}$$

$$C_{ns+5,ns+1} = (i\alpha_0 + m_{13})\sum_{s=1}^{ns}\rho_s e_{vs},$$

$$C_{ns+5,ns+2} = (m_{11} + m_{33})\sum_{s=1}^{ns}\rho_s e_{vs} + \frac{d}{dy}\left(\sum_{s=1}^{ns}\rho_s e_{vs}\right),$$

$$C_{ns+5,ns+3} = i\beta_0\sum_{s=1}^{ns}\rho_s e_{vs},$$

$$C_{ns+5,ns+4} = -\frac{d}{dy}\left(\frac{dT_V}{dy}\frac{\partial k_V}{\partial T}\right) - \frac{\partial Q_{T-V}}{\partial T} - \sum_{s=1}^{ns} e_{vs}\frac{\partial \omega_s}{\partial T} + \frac{d}{dy}\left[\sum_{s=1}^{ns} e_{vs}\left(c_s\frac{d\rho}{dy} - \frac{d\rho_s}{dy}\right)\frac{\partial D_s}{\partial T}\right]$$

$$+ (m_{11}+m_{33})\left[\sum_{s=1}^{ns} e_{vs}\left(c_s\frac{d\rho}{dy} - \frac{d\rho_s}{dy}\right)\frac{\partial D_s}{\partial T} - \frac{dT_V}{dy}\frac{\partial k_V}{\partial T}\right],$$

$$C_{ns+5,ns+5} = i\left[\alpha_0\left(u\sum_{s=1}^{ns}\rho_s\frac{\partial e_{vs}}{\partial T_V} - m_{13}k_V\right) - \omega\sum_{s=1}^{ns}\rho_s\frac{\partial e_{vs}}{\partial T_V}\right] - \frac{dQ_{T-V}}{dy} - \sum_{s=1}^{ns} e_{vs}\frac{\partial \omega_s}{\partial T_V} - \sum_{s=1}^{ns}\omega_s\frac{\partial e_{vs}}{\partial T_V}$$

$$+ \left(m_{13}u + (m_{11}+m_{33})v + \frac{dv}{dy}\right)\sum_{s=1}^{ns}\rho_s\frac{\partial e_{vs}}{\partial T_V} - \frac{d}{dy}\left(\frac{dT_V}{dy}\frac{\partial k_V}{\partial T_V}\right) + \left(\alpha_0^2+\beta_0^2\right)k_V$$

$$+ \frac{d}{dy}\left[\sum_{s=1}^{ns} D_s\left(c_s\frac{d\rho}{dy} - \frac{d\rho_s}{dy}\right)\frac{\partial e_{vs}}{\partial T_V}\right] + v\frac{d}{dy}\left(\sum_{s=1}^{ns}\rho_s\frac{\partial e_{vs}}{\partial T_V}\right) + (m_{11}+m_{33})\left[\sum_{s=1}^{ns} D_s\left(c_s\frac{d\rho}{dy} - \frac{d\rho_s}{dy}\right)\frac{\partial e_{vs}}{\partial T_V} - \frac{dT_V}{dy}\frac{\partial k_V}{\partial T_V}\right].$$

APPENDIX B: LST SHOCK BOUNDARY CONDITION MATRIX ELEMENTS

The nonzero elements of each complex matrix for the nonequilibrium LST shock boundary conditions are given below, where $\vec{\phi} = [\hat{\rho}_1, \hat{\rho}_2, \ldots, \hat{\rho}_{ns}, \hat{u}, \hat{v}, \hat{w}, \hat{T}, \hat{T}_V]^T$ and δ_{ij} is the Kronecker delta. The subscripts i, j = 1, 2, ... , ns, where ns is the number of species in the model. The overbars indicating the steady mean flow components have been dropped for simplicity.

The shock boundary equations are repeated here for clarity,

$$\sum_{j=1}^{ns+5} \hat{B}_{ij}\hat{\phi}_j = 0, \quad i = 1, 2, \ldots, ns+4.$$

This represents ns + 4 equations for ns + 5 independent variables, and therefore an additional equation is required to close the system. The closure equations considered were mixture continuity, y-momentum, and the right-running characteristic equations. The following simplifying terms are introduced:

$$X_s = i\alpha\Delta(\rho_s u) - i\omega\Delta(\rho_s), \quad s = 1, 2, \ldots, ns,$$

$$X_{ns+1} = i\alpha\Delta(\rho u^2 + p) - i\omega\Delta(\rho u),$$

$$X_{ns+2} = i\alpha\Delta(\rho u v) - i\omega\Delta(\rho v),$$

$$X_{ns+3} = i\beta\Delta p,$$

$$X_{ns+4} = i\alpha\Delta(u(\rho e + p)) - i\omega\Delta(\rho e),$$

$$X_{ns+5} = i\alpha\Delta(u\rho e_v) - i\omega\Delta(\rho e_v),$$

where $\Delta()$ is the jump condition across the shock. For example, $\Delta(\rho u) = (\rho u)_\infty - (\rho u)_{shock}$ where the subscript ∞ denotes upstream of the shock and *shock* denotes immediately downstream of the shock. The nonzero components of $\hat{B}$ are

$$\hat{B}_{i,j} = X_{ns+1}\delta_{ij}(au - v) - X_i\left(a\frac{\mathcal{R}}{M_j}T + au^2 - uv\right),$$

$$\hat{B}_{i,ns+1} = X_{ns+1}a\rho_i - X_i(2a\rho u - \rho v),$$

$$\hat{B}_{i,ns+2} = -X_{ns+1}\rho_i + X_i\rho u,$$

$$\hat{B}_{i,ns+4} = -X_i a\frac{p}{T},$$

$$\hat{B}_{ns+1,j} = X_{ns+1}\left(auv - v^2 + \frac{\mathcal{R}}{M_j}T\right) - X_{ns+2}\left(au^2 - uv + a\frac{\mathcal{R}}{M_j}T\right),$$

$$\hat{B}_{ns+1,ns+1} = X_{ns+1}a\rho v + X_{ns+2}(\rho v - 2a\rho u),$$

$$\hat{B}_{ns+1,ns+2} = X_{ns+1}(a\rho u - 2\rho v) + X_{ns+2}\rho u,$$

$$\hat{B}_{ns+1,ns+4} = -X_{ns+1}\frac{p}{T} - X_{ns+2}a\frac{p}{T},$$

$$\hat{B}_{ns+2,j} = X_{ns+3}\left(uv - a\frac{\mathcal{R}}{M_j}T - au^2\right),$$

$$\hat{B}_{ns+2,ns+1} = X_{ns+3}(\rho v - 2a\rho u),$$

$$\hat{B}_{ns+2,ns+2} = X_{ns+3}\rho u,$$

$$\hat{B}_{ns+2,ns+3} = a\rho u - \rho v,$$

$$\hat{B}_{ns+2,ns+4} = -X_{ns+3}a\frac{p}{T},$$

$$\hat{B}_{ns+3,j} = X_{ns+1}(au - v)\left[c_{v,j}T + e_{vj} + \frac{1}{2}(u^2+v^2) + h_j^o + \frac{\mathcal{R}}{M_j}T\right] - X_{ns+4}\left(a\frac{\mathcal{R}}{M_j}T - uv + au^2\right),$$

$$\hat{B}_{ns+3,ns+1} = X_{ns+1}[(au - v)\rho u + a(\rho e + p)] + X_{ns+4}(\rho v - 2a\rho u),$$

$$\hat{B}_{ns+3,ns+2} = X_{ns+1}[(au - v)\rho v - (\rho e + p)] + X_{ns+4}\rho u,$$

$$\hat{B}_{ns+3,ns+4} = X_{ns+1}(au - v)\left[\rho c_v + \frac{p}{T}\right] - X_{ns+4}a\frac{p}{T},$$

$$\hat{B}_{ns+3,ns+5} = (au - v)\sum_{s=1}^{ns}\rho_s\frac{\partial e_{vs}}{\partial T_V},$$

$$\hat{B}_{ns+4,j} = X_{ns+1}(au - v)e_{vj} - X_{ns+5}\left(a\frac{\mathcal{R}}{M_j}T - uv + au^2\right),$$

$$\hat{B}_{ns+4,ns+1} = X_{ns+1}a\rho e_v + X_{ns+5}(\rho v - 2a\rho u),$$

$$\hat{B}_{ns+4,ns+2} = -X_{ns+1}\rho e_v + X_{ns+5}\rho u,$$

$$\hat{B}_{ns+4,ns+4} = -X_{ns+5}a\frac{p}{T},$$

$$\hat{B}_{ns+4,ns+5} = (au - v)\sum_{s=1}^{ns}\rho_s\frac{\partial e_{vs}}{\partial T_V}.$$

REFERENCES

[1]E. Reshotko, "Hypersonic stability and transition," in *Hypersonic Flows for Reentry Problems* (Springer-Verlag, Berlin, 1991), Vol. 1, pp. 18–34.

[2]X. Zhong and X. Wang, "Direct numerical simulation on the receptivity, instability, and transition of hypersonic boundary layers," Annu. Rev. Fluid Mech. **44**, 527–561 (2012).

[3]A. Fedorov, "Transition and stability of high-speed boundary layers," Annu. Rev. Fluid Mech. **43**, 79–95 (2011).

[4]L. M. Mack, "Boundary layer linear stability theory," AGARD Technical Report No. 709, 1984.

[5]A. Fedorov and A. Tumin, "High-speed boundary-layer instability: Old terminology and a new framework," AIAA J. **49**, 1647–1657 (2011).

[6]M. V. Morkovin, "Transition at hypersonic speeds," Technical Report ICASE Interim Report 1, NASA Contractor Report 178315, ICASE, NASA Langley Research Center, NASA Langley Research Center, Hampton, VA, 1987.

[7]L. M. Mack, "On the inviscid acoustic-mode instability of supersonic shear flows. I. Two-dimensional waves," Theor. Comput. Fluid Dyn. **2**, 97–123 (1990).

[8]V. Gushchin and A. Fedorov, "Asymptotic analysis of inviscid perturbations in a supersonic boundary layer," J. Appl. Mech. Tech. Phys. **30**, 64–70 (1989).

[9]A. Demetriades, "Hypersonic viscous flow over a slender cone. III. Laminar instability and transition," AIAA Paper No. 74-535, 1974.

[10]C.-H. Zhang, Q. Tang, and C.-B. Lee, "Hypersonic boundary-layer transition on a flared cone," Acta Mech. Sin. **29**, 48–53 (2013).

[11]X. Zhong and Y. Ma, "Boundary-layer receptivity of Mach 7.99 flow over a blunt cone to free-stream acoustic waves," J. Fluid Mech. **556**, 55–103 (2006).

[12]N. Parsons, X. Zhong, J. Kim, and J. Eldredge, "Numerical study of hypersonic receptivity with thermochemical non-equilibrium on a blunt cone," AIAA Paper 2010-4446, 2010.

[13]D. Heitmann and R. Radespiel, "Simulation of the interaction of a laser generated shock wave with a hypersonic conical boundary layer," AIAA Paper 2011-3875, 2011.

[14]Y. Ma and X. Zhong, "Receptivity of a supersonic boundary layer over a flat plate. I. Wave structures and interactions," J. Fluid Mech. **488**, 31–78 (2003).

[15]M. R. Malik, "Numerical methods for hypersonic boundary layer stability," J. Comput. Phys. **86**, 376–413 (1990).

[16]G. Stuckert and H. Reed, "Linear disturbances in hypersonic, chemically reacting shock layers," AIAA J. **32**, 1384–1393 (1994).

[17]M. L. Hudson, N. Chokani, and G. Candler, "Linear stability of hypersonic flow in thermochemical nonequilibrium," AIAA J. **35**, 958–964 (1997).

[18]H. B. Johnson, T. G. Seipp, and G. Candler, "Numerical study of hypersonic reacting boundary layer transition on cones," Phys. Fluids **10**, 2676–2685 (1998).

[19]H. B. Johnson and G. Candler, "Hypersonic boundary layer stability analysis using PSE-Chem," AIAA Paper 2005-5023, 2005.

[20]H. B. Johnson and G. Candler, "Analysis of laminar-turbulent transition in hypersonic flight using PSE-Chem," AIAA Paper 2006-3057, 2006.

[21]L. Mack, "Review of linear compressible stability theory," in *Stability of Time Dependent and Spatially Varying Flows*, edited by D. Dwoyer and M. Hussaini (Springer-Verlag, 1985), pp. 164–187.

[22]M. M. Sherman and T. Nakamura, "Flight test measurements of boundary-layer transition on a nonablating 22° cone," J. Spacecr. Rockets **7**, 137–142 (1970).

[23]M. R. Malik, "Hypersonic flight transition data analysis using parabolized stability equations with chemistry effects," J. Spacecr. Rockets **40**, 332–344 (2003).

[24]L. Lees, "The stability of the laminar boundary layer in a compressible fluid," Technical Report No. 876, NACA, 1947.

[25]L. Mack, "Effect of cooling on boundary-layer stability at Mach number 3," in *Instabilities and Turbulence in Engineering Flows*, edited by D. Ashpis, T. Gatski, and R. Hirsch (Springer-Verlag, 1993).

[26]N. Bitter and J. Shepherd, "Stability of highly cooled hypervelocity boundary layers," J. Fluid Mech. **778**, 586–620 (2015).

[27]P. Chuvakhov and A. Fedorov, "Spontaneous radiation of sound by instability of a highly cooled hypersonic boundary layer," in 8th AIAA Flow Control Conference, 2016.

[28]P. Chuvakhov and A. Fedorov, "Spontaneous radiation of sound by instability of a highly cooled hypersonic boundary layer," J. Fluid Mech. **805**, 188–206 (2016).

[29]C.-L. Chang, H. Vinh, and M. Malik, "Hypersonic boundary-layer stability with chemical reactions using PSE," in 28th AIAA Fluid Dynamics Conference, Snowmass Village, CO, USA, 1997.

[30]A. Fedorov, G. Bres, M. Inkman, and T. Colonius, "Instability of hypersonic boundary layer on a wall with resonating micro-cavities," in 49th AIAA Aerospace Sciences Meeting, 2011.

[31]R. Wagnild, "High enthalpy effects on two boundary layer disturbances in supersonic and hypersonic flow," Ph.D. thesis, University of Minnesota, Minneapolis, MN, 2012.

[32]G. Bres, M. Inkman, T. Colonius, and A. Fedorov, "Second-mode attenuation and cancellation by porous coatings in a high-speed boundary layer," J. Fluid Mech. **726**, 312–337 (2013).

[33]J. Klentzman and A. Tumin, "Stability and receptivity of high speed boundary layers in oxygen," AIAA Paper 2013-2882, 2013.

[34]J. Jewell, "Boundary-layer transition on a slender cone in hypervelocity flow with real gas effects," Ph.D. thesis, California Institute of Technology, 2014.

[35]A. Fedorov, V. Soudakov, and I. Leyva, "Stability analysis of high-speed boundary-layer flow with gas injection," in 7th AIAA Theoretical Fluid Mechanics Conference, 2014.

[36]L. Salemi, H. Fasel, S. Wernz, and E. Marquart, "Numerical investigation of wave-packets in a hypersonic high-enthalpy boundary-layer on a 5 degree sharp cone," in 7th AIAA Theoretical Fluid Mechanics Conference, 2014.

[37]L. Salemi, H. Fasel, S. Wernz, and E. Marquart, "Numerical investigation of nonlinear wave packets in a hypersonic high-enthalpy boundary layer on a 5 degree sharp cone," in 45th AIAA Thermophysics Conference, 2015.

[38]L. Salemi and H. Fasel, "Linearized Navier-Stokes simulations of the spatial stability of a hypersonic boundary-layer on a flared cone," in 53rd AIAA Aerospace Sciences Meeting, 2015.
[39]L. Salemi, A. Gross, H. Fasel, S. Wernz, and E. Marquart, "Linearized Navier-Stokes calculations of the spatial stability of a hypersonic boundary layer on a 5° sharp cone with high temperature effects," in 52nd Aerospace Sciences Meeting, 2014.
[40]L. Salemi, "Numerical investigation of hypersonic conical boundary-layer stability including high-enthalpy and three-dimensional effects," Ph.D. thesis, University of Arizona, 2016.
[41]A. Sescu, J. Sawaya, V. Sassanis, and M. Visbal, "Study of the effect of two-dimensional wall non-uniformities on high-speed boundary layers," AIAA Paper 2017-4511, 2017.
[42]L. Edwards and A. Tumin, "Real gas effects on receptivity to kinetic fluctuations. I. Mean flow effect," AIAA Paper 2017-0070, 2017.
[43]C. Knisely and X. Zhong, "Supersonic modes in hot-wall hypersonic boundary layers with thermochemical nonequilibrium effects," AIAA Paper 2018-2085, 2018.
[44]C. Knisely and X. Zhong, "The supersonic mode and the role of wall temperature in hypersonic boundary layers with thermochemical nonequilibrium effects," AIAA Paper 2018-3218, 2018.
[45]C. H. Mortensen, "Toward an understanding of supersonic modes in boundary-layer transition for hypersonic flow over blunt cones," J. Fluid Mech. **846**, 789–814 (2018).
[46]C. Knisely and X. Zhong, "An investigation of sound radiation by supersonic unstable modes in hypersonic boundary layers," AIAA Paper 2017-4516, 2017.
[47]A. Tumin, private communication (2016).
[48]C. H. Mortensen and X. Zhong, "High-order shock-fitting method for hypersonic flow with graphite ablation and boundary layer stability," AIAA Paper 2012-3150, 2012.
[49]C. H. Mortensen and X. Zhong, "Numerical simulation of graphite ablation induced outgassing effects on hypersonic boundary layer receptivity over a cone frustum," AIAA Paper 2013-0522, 2013.
[50]C. H. Mortensen and X. Zhong, "Real gas and surface ablation effects on hypersonic boundary layer instability over a blunt cone," AIAA Paper 2013-2981, 2013.
[51]C. H. Mortensen and X. Zhong, "Simulation of second-mode instability in a real-gas hypersonic flow with graphite ablation," AIAA J. **52**, 1632–1652 (2014).
[52]C. H. Mortensen and X. Zhong, "Numerical simulation of hypersonic boundary-layer instability in a real gas with two-dimensional surface roughness," AIAA Paper 2015-3077, 2015.
[53]C. H. Mortensen, "Effects of thermochemical nonequilibrium on hypersonic boundary-layer instability in the presence of surface ablation and isolated two-dimensional roughness," Ph.D. thesis, University of California Los Angeles, 2015.
[54]J. Williamson, "Low-storage Runge-Kutta schemes," J. Comput. Phys. **35**, 48–56 (1980).
[55]M. Malik and R. Spall, "On the stability of compressible flow past axisymmetric bodies," J. Fluid Mech. **228**, 443–463 (1991).
[56]E. Anderson, Z. Bai, C. Bischof, S. Blackford, J. Demmel, J. D. Garra, J. D. Croz, A. Greenbaum, S. Hammarling, A. McKenney, and D. Sorensen, *LAPACK Users' Guide*, 3rd ed. (Society for Industrial and Applied Mathematics, Philadelphia, PA, 1999).
[57]C.-L. Chang, M. Malik, and M. Hussaini, "Effects of shock on the stability of hypersonic boundary layers," in 21st AIAA Plasma Dynamics and Lasers Conference, 1990.
[58]M. L. Hudson, "Linear stability of hypersonic flows in thermal and chemical nonequilibrium," Ph.D. thesis, North Carolina State University, 1996.
[59]A. Fedorov and A. Tumin, "Initial-value problem for hypersonic boundary-layer flows," AIAA J. **41**, 379–389 (2003).
[60]A. Fedorov, "Receptivity of a high-speed boundary layer to acoustic disturbances," J. Fluid Mech. **491**, 101–129 (2003).
[61]P. Balakumar and M. R. Malik, "Discrete modes and continuous spectra in supersonic boundary layers," J. Fluid Mech. **239**, 631–656 (1992).
[62]P. Gaydos and A. Tumin, "Multimode decomposition in compressible boundary layers," AIAA J. **42**, 1115–1121 (2004).
[63]A. Tumin, "Three-dimensional spatial normal modes in compressible boundary layers," AIAA Paper 2006-1109, 2006.
[64]A. Tumin, "Three-dimensional spatial normal modes in compressible boundary layers," J. Fluid Mech. **586**, 295–322 (2007).
[65]C. P. Knisely and X. Zhong, "Sound radiation by supersonic unstable modes in hypersonic blunt cone boundary layers. II. Direct numerical simulation," Phys. Fluids **31**, 024104 (2019).